# Multi-IRS Assisted Multi-Cluster Wireless Powered IoT Networks

Zheng Chu, *Member, IEEE*, Pei Xiao, *Senior Member, IEEE*
De Mi, *Senior Member, IEEE*, Wanming Hao, *Member, IEEE*
Yue Xiao, *Member, IEEE*, and Lie-Liang Yang, *Fellow, IEEE*

***Abstract*—This paper proposes a multi-cluster wireless powered Internet of Things (WP-IoT) network assisted by multiple intelligent reflecting surfaces (multi-IRS). In this network, a power station (PS) first broadcasts wireless energy to the distributed IoT devices grouped into multiple clusters. The IoT devices then use the harvested energy to convey their information to an access point (AP), based on a hybrid time- and frequency-division multiple access (TDMA-FDMA) protocol. Furthermore, multiple IRSs are deployed to perform anomalous reflection for energy and information transfer, to improve energy harvesting and data transmission capabilities. Under the constraints of the unit-modulus phase shifts, the transmission time shared among clusters and the bandwidth shared by the devices in each cluster, the considered system is optimized by maximizing its sum throughput. The optimization problem is non-convex and with complicatedly coupled variables. To solve this problem, we propose to first apply the Lagrange dual method and the Karush-Kuhn-Tucker (KKT) conditions to derive closed-form solutions for transmission scheduling and bandwidth allocation, then the quadratic transformation (QT) and the alternating optimization (AO) algorithm are introduced to solve the downlink and uplink IRS phase shifts, whilst the Majorization-Minimization (MM) and Riemannian Manifold Optimization (RMO) methods are applied to iteratively derive their closed-form solutions. Additionally, we provide a benchmark scheme to facilitate the system design, where each IRS can control its "on/off" state to aid the downlink and uplink transmissions in the condition of at most one activated IRS during one certain time duration. Finally, simulation results are presented to verify the optimality of our proposed scheme and highlight the beneficial role of the IRS.**

***Index Terms*—Intelligent reflecting surface (IRS), wireless powered Internet of Things (WP-IoT) network, fractional energy harvesting, hybrid TDMA-FDMA, Majorization-Minimization (MM) and Riemannian Manifold Optimization (RMO).**

## I. Introduction

For next-generation wireless networks, an intelligent radio environment has attracted fast-growing attention from academia and industry due to its holographic mode. This environment introduces novel meta-surfaces to passively reflect the intended signals from the transmitter to the desired receiver via the surfaces, referred to as intelligent reflecting surfaces (IRSs) [1], [2]. In structure, each IRS is composed of massive reflecting elements with low-cost and small-size features, managed by a smart controller for simultaneously information reception and passive reflection. Each reflecting element induces a reflection coefficient to control the radio wave such that the reflected signals are coherently added at the receiver [3]. Therefore, the intelligent radio environment can effectively enhance spectral efficiency or throughput without altering the existing communication network architectures and the requirement of extra energy consumption.

On the other hand, Internet of Things (IoT) has been experiencing an explosive demand requiring massive connections of myriads of wireless devices (WDs), including, smartphones, wearable devices, sensors, etc., whereas most of these devices are vulnerable to the constrained energy to support their information transmission. In many applications, regular battery maintenance or replacement, as the traditional endeavour to extend the operational lifetime of IoT devices, might not be feasible, since the IoT devices may be deployed in extreme environments for remote monitoring of emergency services. Furthermore, the energy-efficient management schemes designed for the existing IoT networks may induce a high algorithmic complexity and also can be challenging for the configurations of the IoT sensors' hardware architectures [4]. To address the energy-constrained issue, radio frequency (RF) wireless energy transfer (WET) has been promoted, which exploits the far-field propagation properties of electromagnetic wave (EW) to extract energy wirelessly [5], [6]. The RF-WET has recently emerged as a promising technique, namely, the wireless powered communication network (WPCN), equipping one or more dedicated energy source(s) to sustainably provide WET to the WDs, thus, prolong WDs' battery life and reduce the cost of maintenance and replacement [5]. The WDs can harvest energy from the RF environment, to support their wireless information transfer (WIT). Typically, the "*harvest-then-transmit*" protocol is used in WPCN to schedule the time durations for WET and WIT and effectively circumvent the interference between WDs [7].

### A. State-of-the-Art

Recently, the integration of WPCN with IRS has been promoted as a revolutionized paradigm in wireless-powered IoT (WP-IoT) networks, where the design principle is to improve the network throughput and energy efficiency of the WPCN simultaneously with aid of the IRS to coordi-

This work was supported in part by the U.K. Engineering and Physical Sciences Research Council (EPSRC) under Grants EP/X013162/1.

Z. Chu, P. Xiao, and D. Mi are with 5GIC & 6GIC, Institute for Communication Systems (ICS), University of Surrey, Guildford GU2 7XH, UK. (Email: andrew.chuzheng7@gmail.com, p.xiao@surrey.ac.uk, d.mi@surrey.ac.uk)

W. Hao is with the School of Information Engineering, Zhengzhou University, Zhengzhou 450001, China. (Email: iewmhao@zzu.edu.cn)

Y. Xiao is with the National Key Laboratory of Science and Technology on Communications, University of Electronic Science and Technology of China, Chengdu 611731, China. (Email: xiaoyue@uestc.edu.cn)

L. Yang is with the School of Electronics and Computer Science, University of Southampton, Southampton SO17 1BJ, U.K. (Email: lly@ecs.soton.ac.uk)

nate its beam patterns. The existing works in literature have studied some IRS-assisted simultaneous wireless information and power transfer (SWIPT) systems [8]–[10]. Specifically, in [8], IRS was applied to a multiple-input single-output (MISO) SWIPT downlink system. The active beamformers for information and energy transmissions as well as the passive IRS phase shifts were jointly optimized to achieve the maximum weighted sum harvested power (WSHP). The benefits introduced by IRS were highlighted via a rate-energy (R-E) trade-off metric. The system in [8] was extended to the case using distributed IRSs in [9] for transmit power minimization (TPM), where the optimization problem was iteratively solved by a penalty-based approach. It was confirmed that an energy-efficiency gain can be obtained by IRS. In [10], a multiple-input multiple-output (MIMO) SWIPT system with a single IRS was investigated, supported by solving a weighted sum rate maximization (WSRM) problem that was decomposed into several subproblems to separately optimize the transmit precoders and the IRS phase shifts, but iteration between them is achieved via the block coordinate descent (BCD) algorithm.

The coordination between IRS and WPCN has been introduced to IoT networks to improve system throughput and energy efficiency [11]–[15]. In [11], an IRS first assisted the energy harvesting of IoT devices by reflecting the energy signals radiated from a power station (PS). Then, the individual device utilized its harvested energy to deliver information to an access point (AP) with the assistance of the IRS, based on time-division multiple access (TDMA). To demonstrate the overall performance, the sum throughput was maximized to optimally schedule the transmission time slots and set the IRS phase shifts for downlink WET and uplink WIT. Moreover, two novel protocols, named time switching and power splitting, were proposed to harvest the RF energy at the IRS for its control circuit operation [12], [13]. Specifically, semidefinite programming (SDP) relaxation and one-dimensional (1-D) line approach were adopted to numerically solve the sum throughput maximization problem [12]. In [13], a novel low-complexity scheme was proposed to optimally derive the closed-form solutions for the time scheduling and IRS phase shifts, which was verified to achieve comparable performance with the numerical approaches. In [14], non-orthogonal multiple access (NOMA) scheme was introduced in an IRS-assisted WPCN, which optimized the IRS passive beamforming to maximize the sum throughput. In [14], a closed-form solution for the IRS passive beamforming was attained via an iterative algorithm based on alternating optimization (AO) algorithm. A similar approach was applied to multi-cluster cases in [15], where a plethora of IoT devices were grouped into different clusters, and each cluster is TDMA-based with the IoT devices sharing one sub-time slot for information transfer via NOMA. The study demonstrated that the hybrid TDMA and NOMA protocol is capable of achieving a good performance-complexity trade-off.

Despite the considerable efforts to research the IRS-aided WP-IoT networks, the focus so far is mainly on the investigation of multiple IoT devices in a single cluster suffering from the energy-constrained issue. In addition, an ideal yet over-simplified linear model is typically employed to characterize the energy harvesting at IoT devices. There is also a research gap on using multiple IRSs (or multi-IRS) in a distributed manner where each IRS can control its "on/off" state to serve the IoT devices nearby, which can be a promising solution to extend the network coverage and enhance throughput, Inspired by these research motivations, we propose a multi-IRS assisted multi-cluster WP-IoT network, where multiple IRSs are deployed to participate in energy harvesting and information transmission. It constitutes a novel paradigm to optimally coordinate energy and information transmissions of different clusters of IoT devices. *The contributions of this paper are summarized as follows:*

1) Firstly, a multi-IRS-assisted multi-cluster WP-IoT network is proposed. Specifically, in the downlink WET, a PS wirelessly radiates RF energy to IoT devices that are grouped into multiple clusters. Then, in the uplink WIT, these devices utilize the harvested energy to deliver their individual information to the AP in a hybrid TDMA-FDMA fashion, where a dedicated time slot is scheduled for every cluster via TDMA and dedicated bandwidth is allocated for each device in each cluster via FDMA. Meanwhile, multiple IRSs passively participate in the energy/information reflection for downlink WET and uplink WIT to improve energy harvesting and information transmission capabilities. To the best of the authors' knowledge, there are only a few existing works that have investigated the multi-IRS-assisted multi-cluster WP IoT network.
2) Secondly, the overall performance of the system model under investigation is evaluated, where all IRSs participate in energy/information reflection in the downlink WET/uplink WIT. This involves a maximization problem formulation of the sum throughput, subject to the constraints of IRS beam patterns, time scheduling, and bandwidth allocation. The formulated problem includes a sum of logarithm functions with multiple fractional programs (MFPs) with coupled variables and a unit-modulus IRS phase shift constraint, leading to a non-convex issue and cannot be solved directly. The existing works such as [14]–[16] rely on the SDP relaxation, sequential rank-one constraint relaxation (SROCR), and successive convex approximation (SCA) techniques to reformulate the non-convex problem into a convex one that can be numerically solved by interior-point method [17]. This work aims to facilitate the optimal design of the IRS beamforming, and we propose to use the Lagrange dual method with Karush-Kuhn-Tucker (KKT) conditions, which derives the closed-form solutions of time scheduling and bandwidth allocation and reformulates the sum of logarithm functions into a sum of MFPs, proceeding to a quadratic transformation (QT) for reformulation from a sum of fractional functions to a subtractive form for the sake of tractability. Then, majorization-minimization (MM) and Riemannian manifold optimization (RMO) approaches are adopted to iteratively derive the closed-form of the downlink and uplink IRS beam patterns.
3) Thirdly, a benchmark scheme, namely, IRS selection, is

conceived to facilitate network design, which is based on the premise that each IRS can control its "on/off" state. Given a dedicated time period, only one IRS is activated to participate in the downlink WET or uplink WIT. For this configuration, a binary time scheduling vector is induced to recast the formulated problem into a linear programming (LP).

The remainder of this paper is organized as follows: Section II describes the considered system model and formulates the sum throughput maximization problem. The optimal solution of this problem is investigated in Section III. The benchmark scheme is exploited in Section IV. Numerical results are demonstrated in Section V, and Section VI concludes this paper. Here, Table I summarizes of notations being used in this paper.

## II. System Model

We investigate a multi-IRS assisted multi-cluster WP-IoT network as shown in Fig. 1. Specifically, in total $Q$ IoT devices are grouped into $K$ clusters, and each cluster consists of $Q_k,\ \forall k \in [1,K]$ IoT devices, i.e., $\sum_{k=1}^{K} Q_k = Q$. $\mathcal{D}_{k,q},\ \forall k \in [1,K],\ \forall q \in [1,Q_k]$ represents the $q$-th IoT devices of the $k$-the cluster. We assume that multiple IRSs are deployed to passively reflect the energy or information signals by controlling their own reflecting coefficients. Each IRS is equipped with $N_l$ reflecting elements $\forall l \in [1,L]$, satisfying $\sum_{l=1}^{L} N_l = N$, whereas other devices (i.e., PS, IoT devices, AP) are equipped with single antenna each. During the downlink WET, the PS wirelessly charges these groups of IoT devices. During the uplink WIT, these devices use the harvested energy to deliver their individual information to the AP, for which a hybrid TDMA-FDMA protocol is adopted, as shown in Fig. 2. Specifically, we divide the time resource into periods, and in each period $T$, the downlink WET time duration is set to $\tau_0$, and the uplink WIT time duration of each cluster is given as $\tau_k$. Within a cluster and a time duration of $\tau_k$, the IoT devices share the total bandwidth $B$ to deliver their information to the AP, with the $q$-th device assigned a bandwidth of $w_q,\ \forall q \in [1,Q_k],\ \forall k \in [1,K]$, which satisfies that $\sum_{q=1}^{Q_k} w_q = B$.

In addition, we denote $\mathbf{\Theta}_{l,k} = \text{diag}\left[\theta_{k,1},...,\theta_{k,N_l}\right]$, $\theta_{k,n} = \beta_{k,n_l}\exp(j\alpha_{k,n_l})$ as the $l$-th IRS phase shift matrix serving the $k$-th cluster, where $\beta_{k,n_l} \in [0,1]$ and $\alpha_{k,n_l} \in [0,2\pi]$, $\forall n_l \in [1,N_l],\ \forall k \in [0,K]$, denote the amplitude and phase shift of the corresponding reflecting element.[1] In practice, the phase shift of each IRS element is dynamically adjusted, coordinated by the IRS controller. When an IRS aims to participate in the downlink WET, it requires energy collection to support the circuit operation at its controller. To fulfil this technical requirement, our prior works have presented two energy harvesting frameworks at the IRS, i.e., time switching [13] and power splitting [18]. The focus of this work is on developing a suitable optimization algorithm for the IRS passive beam patterns and the transmission framework. To this end, a general approach is to investigate the upper bounds of the sum throughput performance of the system model, by assuming the channel state information (CSI) perfectly available. To elaborate more on the CSI acquisition: channel estimation algorithms have been presented in [19], [20] to acquire the cascaded CSI of the IRS-related links by utilizing the passive pilots and message passing algorithms, respectively; the effect of the imperfect cascaded CSI has been investigated in [21]–[23], where it typically obeys bounded and statistical CSI uncertainties. Considering the assumption of the imperfect CSI, there works characterized the worst-case and outage probability robust beamforming designs to maximize achievable rate and minimize transmit power at the AP, respectively, which can be tackled by using robust resource allocations to alternately optimize active transmit precoding and passive reflecting beamforming. The CSI uncertainty can significantly increase network energy consumption or degrade the achievable rate or system throughput [21]–[23].

[1]To maximize the sum throughput, it requires a maximum energy and/or information signal reflection of IRSs. For simplicity, each element of the IRSs is set to have $\beta_{k,n_l} = 1$, to maximize the reflection gain.

Table II shows the notations of channel coefficients. For the downlink WET, a widely considered linear energy harvesting model is used, and the energy harvested by $\mathcal{D}_{k,q}$ is given as

$$E_{k,q}^{linear} = \eta\tau_0 P_0 \left| g_{d,k,q} + \sum_{l=1}^{L} \mathbf{g}_{0,l}\mathbf{\Theta}_{0,l}\mathbf{g}_{r,l,k,q} \right|^2, \quad (1)$$

where $\eta \in (0,1]$ denotes the energy conversion efficiency, and $P_0$ is the transmit power of PS. Note that $E_{k,q}^{linear}$ in (1) can be treated as a linear function with respect to the term $P_0|g_{d,k,q} + \sum_{l=1}^{L} \mathbf{g}_{0,l}\mathbf{\Theta}_{0,l}\mathbf{g}_{r,l,k,q}|^2$, and $\eta$ is a constant aiming to characterize the linear behaviour of a non-linear energy harvester. However, this energy harvester's circuit practically implements the non-linear transform, making the output power a non-linear function with respect to the RF input power [24]. In this paper, we propose a fractional model at IoT devices to characterize the approximated non-linear energy harvesting (NLEH) properties and saturation region of this energy harvester, where the harvested energy at $\mathcal{D}_{k,q}$ is given by

$$E_{k,q}^{nonlinear} = \tau_0 \frac{(a_{k,q}c_{k,q} - b_{k,q})P_0 \left| g_{d,k,q} + \mathbf{g}_0\mathbf{\Theta}_0\mathbf{g}_{r,k,q} \right|^2}{c_{k,q}P_0 \left| g_{d,k,q} + \mathbf{g}_0\mathbf{\Theta}_0\mathbf{g}_{r,k,q} \right|^2 + c_{k,q}^2}, \quad (2)$$

where $a_{k,q} = 2.463$, $b_{k,q} = 1.635$, and $c_{k,q} = 0.826$ are positive constants [25]; $\mathbf{g}_0 = \left[\mathbf{g}_{0,1} \ \cdots \ \mathbf{g}_{0,L}\right]$, $\mathbf{\Theta}_0 = \text{diag}\left[\mathbf{\Theta}_{0,1},\cdots,\mathbf{\Theta}_{0,L}\right]$, and $\mathbf{g}_{r,k,q}^H = \left[\mathbf{g}_{r,1,k,q} \ \cdots \ \mathbf{g}_{r,L,k,q}\right]^H$.

For the uplink WIT, we consider a hybrid TDMA-FDMA protocol to guarantee the connectivity of all IoT devices, where the sum throughput of the $k$-th cluster is given at (3) on the top of the next page, where $\sigma^2$ is the noise power density at the AP, $\mathbf{h}_{k,q} = \left[\mathbf{h}_{k,q,1} \ \cdots \ \mathbf{h}_{k,q,L}\right]$, $\mathbf{\Theta}_k = \text{diag}\left[\mathbf{\Theta}_{k,1},...,\mathbf{\Theta}_{k,L}\right]$, and $\mathbf{h}_r^H = \left[\mathbf{h}_{r,1} \ \cdots \ \mathbf{h}_{r,L}\right]^H$.

### A. Problem Formulation

For the considered system, two types of passive IRS beamformers are covered, i.e., for the downlink and the uplink. We aim to maximize the sum throughput to jointly design the optimal solutions for the passive IRS beamformers $\left(\text{i.e}, \{\mathbf{\Theta}_k\}_{k=0}^K\right)$, transmission time scheduling $\left(\text{i.e}, \{\tau_k\}_{k=0}^K\right)$,

TABLE I: **Notations**

| Notations | Descriptions | Notations | Descriptions | Notations | Descriptions |
|---|---|---|---|---|---|
| $\mathbf{X}$ | A matrix | $\mathbf{x}$ | A vector | conj$(\cdot)$ | Conjugate operator |
| $(\cdot)^H$ | Conjugate transpose operator | $\lvert\cdot\rvert$ | Absolute operator | $\lVert\cdot\rVert$ | Euclidean norm operator |
| $\mathbf{I}_{N\times N}$ | An identity matrix with size $N$ | exp$(\cdot)$ | Exponential function | arg | Phase operation |
| $\mathcal{W}(\cdot)$ | Lambert $\mathcal{W}$ function | $\Re\{\cdot\}$ | Real part of a complex number | diag$[\cdot]$ | Diagonalization operator |

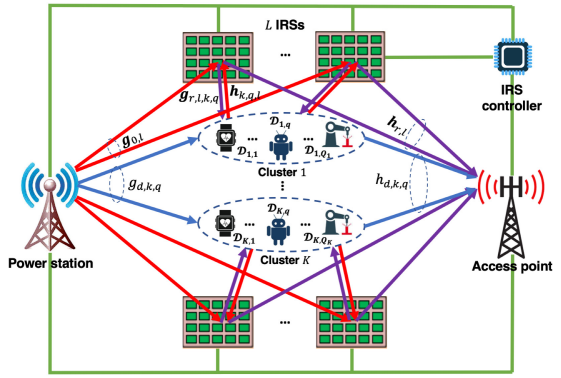


Fig. 1: System model.

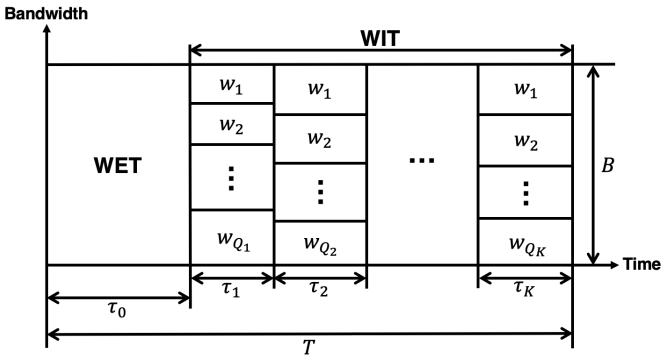


Fig. 2: The hybrid TDMA-FDMA protocol.

TABLE II: **Notations of channel coefficients**

| Notations | Descriptions | Notations | Descriptions | Notations | Descriptions |
|---|---|---|---|---|---|
| $g_{d,k,q}\in\mathbb{C}^{1\times 1}$ | PS to $\mathcal{D}_{k,q}$ | $\mathbf{g}_{0,l}\in\mathbb{C}^{1\times N_l}$ | PS to the $l$-th IRS | $\mathbf{g}_{r,l,k,q}\in\mathbb{C}^{N_l\times 1}$ | The $l$-th IRS to $\mathcal{D}_{k,q}$ |
| $h_{d,k,q}\in\mathbb{C}^{1\times 1}$ | $\mathcal{D}_{k,q}$ to AP | $\mathbf{h}_{k,q,l}\in\mathbb{C}^{1\times N_l}$ | $\mathcal{D}_{k,q}$ to the $l$-th IRS | $\mathbf{h}_{r,l}\in\mathbb{C}^{N_l\times 1}$ | The $l$-th IRS to AP |

$$R_k=\tau_k\sum_{q=1}^{Q_k}w_q\log\left(1+\frac{\tau_0(a_{k,q}c_{k,q}-b_{k,q})P_0\left|g_{d,k,q}+\mathbf{g}_0\mathbf{\Theta}_0\mathbf{g}_{r,k,q}\right|^2\left|h_{d,k,q}+\mathbf{h}_{k,q}\mathbf{\Theta}_k\mathbf{h}_r\right|^2}{\tau_k\left(c_{k,q}P_0\left|g_{d,k,q}+\mathbf{g}_0\mathbf{\Theta}_0\mathbf{g}_{r,k,q}\right|^2+c_{k,q}^2\right)\sigma^2 w_q}\right), \tag{3}$$

and bandwidth allocation $\left(\text{i.e.,}\{w_q\}_{q=1,k=1}^{Q_k,K}\right)$. The problem can be formulated as:

$$\max_{\mathbf{\Omega}_{TDMA-FDMA}}\ \sum_{k=1}^{K}R_k$$
$$s.t.\ \ |\theta_{k,n}|=1,\forall n\in[1,N],\ \forall k\in[0,K], \tag{4a}$$
$$\sum_{k=0}^{K}\tau_k\le T,\tau_k\ge 0,\ \forall k\in[0,K], \tag{4b}$$
$$\sum_{q=1}^{Q_k}w_q\le B,w_q\ge 0,\ \forall q\in[1,Q_k], \tag{4c}$$

$$\mathbf{\Omega}_{TDMA-FDMA}=\left[\{\mathbf{\Theta}_k\}_{k=0}^{K},\{\tau_k\}_{k=0}^{K},\{w_q\}_{q=1,k=1}^{Q_k,K}\right], \tag{4d}$$

where (4a), (4b), and (4c) denote the constraints of the IRS phase shifts, the transmission time scheduling, and the bandwidth allocation, respectively. Problem (4) includes multiple coupled variables which lead to its non-convexity, and therefore, it cannot be solved directly.

## III. Optimal Resource Allocation Scheme for Problem (4)

In this section, we solve the problem (4) to obtain an optimal resource allocation scheme. Let us denote $\boldsymbol{\theta}_0=[\theta_{0,1},...,\theta_{0,N}]$, $t_{0,k,q}=\left|g_{d,k,q}+\mathbf{g}_0\mathbf{\Theta}_0\mathbf{g}_{r,k,q}\right|^2=\left|g_{d,k,q}+\boldsymbol{\theta}_0\mathbf{a}_{k,q}\right|^2$, $\mathbf{a}_{k,q}=\text{diag}\left(\mathbf{g}_0\right)\mathbf{g}_{r,k,q}$, $t_{1,k,q}=\left|h_{d,k,q}+\mathbf{h}_{k,q}\mathbf{\Theta}_k\mathbf{h}_r\right|^2=\left|h_{d,k,q}+\boldsymbol{\theta}_k\mathbf{b}_{k,q}\right|^2$, and $\mathbf{b}_{k,q}=\text{diag}\left(\mathbf{h}_{k,q}\right)\mathbf{h}_r$, it can be shown that problem (4) is equivalently expressed as

$$\max_{\mathbf{\Omega}_{TDMA-FDMA}}\sum_{k=1}^{K}\tau_k\sum_{q=1}^{Q_k}w_q\log\left(1+\frac{\tau_0(a_{k,q}c_{k,q}-b_{k,q})P_0t_{0,k,q}t_{1,k,q}}{\tau_k\left(c_{k,q}P_0t_{0,k,q}+c_{k,q}^2\right)\sigma^2w_q}\right),$$
$$s.t.\ \text{(4a)},\ \text{(4b)},\ \text{(4c)},$$
$$\mathbf{\Omega}_{TDMA-FDMA}=\left[\{\boldsymbol{\theta}_k\}_{k=0}^{K},\ \{\tau_k\}_{k=0}^{K},\ \{w_q\}_{q=1}^{Q_k}\right], \tag{5}$$

Apparently (5) is still intractable. To solve it, we divide (5) into the following two sub-problems:

1) *Sub-problem 1*:

$$f_k(w_q,\boldsymbol{\theta}_k)=\max_{w_q}\sum_{q=1}^{Q_k}w_q\log\left(1+\frac{\tau_0(a_{k,q}c_{k,q}-b_{k,q})P_0t_{0,k,q}t_{1,k,q}}{\tau_k\left(c_{k,q}P_0t_{0,k,q}+c_{k,q}^2\right)\sigma^2w_q}\right),$$
$$s.t.\ \text{(4a)},\ \text{(4c)}. \tag{6}$$

2) *Sub-problem 2*:

$$\max_{\boldsymbol{\theta}_k,\tau_k}\sum_{k=1}^{K}\tau_kf_k\left(w_q,\boldsymbol{\theta}_k\right),\ s.t.\ \text{(4a)},\ \text{(4b)}. \tag{7}$$

Then, we proceed to solve these two sub-problems to obtain the optimal solutions of $\{w_q\}_{q=1}^{Q_k}$, $\forall k\in[1,K]$, $\{\boldsymbol{\theta}_k\}_{k=0}^{K}$ and $\{\tau_k\}_{k=0}^{K}$.

### A. Optimal Solutions of Bandwidth Allocation and Transmission Time Scheduling

The following *theorem* helps solve (6) to obtain $\{w_q\}_{q=1}^{Q_k}$, $\forall k \in [1, K]$, for given $\{\boldsymbol{\theta}_k\}_{k=0}^{K}$:

*Theorem 1:* The sub-problem (6) can be equivalently formulated as

$$f_k(\boldsymbol{\theta}_k) = \max_{\boldsymbol{\theta}_k} B \log\left(1 + \frac{\sum_{q=1}^{Q_k} A_{k,q}}{B}\right), \ s.t. \ (4a), \quad (8)$$

and the optimal solution of $w_q$ is

$$w_q^* = \frac{A_{k,q} B}{\sum_{q=1}^{Q_k} A_{k,q}}, \quad (9)$$

where $A_{k,q} = \frac{\tau_0 (a_{k,q} c_{k,q} - b_{k,q}) P_0 t_{0,k,q} t_{1,k,q}}{\tau_k \left(c_{k,q} P_0 t_{0,k,q} + c_{k,q}^2\right) \sigma^2}$.

*Proof:* See Appendix A. ∎

As seen from *Theorem* 1, the sub-problem (6) (i.e.,$f(w_q, \boldsymbol{\theta}_k)$) can be simplified into (8) (i.e.,$f(\boldsymbol{\theta}_k)$), which involves $\{\boldsymbol{\theta}_k\}_{k=0}^{K}$ only. Thus, substituting $f(\boldsymbol{\theta}_k)$ into the sub-problem (7) yields

$$\max_{\boldsymbol{\Omega}_{TDMA-FDMA}} \sum_{k=1}^{K} \tau_k B \log\left(1 + \frac{\tau_0 \sum_{q=1}^{Q_k} C_{k,q}}{\tau_k B \sigma^2}\right),$$
$$s.t. \ (4a), \ (4b),$$
$$\boldsymbol{\Omega}_{TDMA-FDMA} = \left[\{\boldsymbol{\theta}_k\}_{k=0}^{K}, \ \{\tau_k\}_{k=0}^{K}\right], \quad (10)$$

where $C_{k,q} = \frac{(a_{k,q} c_{k,q} - b_{k,q}) P_0 t_{0,k,q} t_{1,k,q}}{c_{k,q} P_0 t_{0,k,q} + c_{k,q}^2}$. Since the objective function in (10) is a sum of multiple concave functions, and constraint (4b) is linear, the problem (10) is essentially a convex optimization problem with respect to $\{\tau_k\}_{k=0}^{K}$ for given $\{\boldsymbol{\theta}_k\}_{k=0}^{K}$, which can be simplified as:

*Theorem 2:* Problem (10) is equivalent to the following problem with

$$\max_{\boldsymbol{\theta}_k, \tau_0} f_0\left(\{\boldsymbol{\theta}_k\}_{k=0}^{K}, \tau_0\right)$$
$$= B(T - \tau_0) \log\left(1 + \frac{\tau_0 \sum_{k=1}^{K} \sum_{q=1}^{Q_k} C_{k,q}}{(T - \tau_0) B \sigma^2}\right),$$
$$s.t. \ (4a), \ \tau_0 \in [0, T], \quad (11)$$

and the optimal solution of $\{\tau_k\}_{k=1}^{K}$ is

$$\tau_k^* = \frac{(T - \tau_0) \sum_{q=1}^{Q_k} C_{k,q}}{\sum_{k=1}^{K} \sum_{q=1}^{Q_k} C_{k,q}}. \quad (12)$$

*Proof:* See Appendix B. ∎

It can be observed from *Theorem* 2 that problem (11) includes only $\{\boldsymbol{\theta}_k\}_{k=0}^{K}$ and $\tau_0$, but is still not jointly convex and intractable. To circumvent this issue, we start with the derivation of a closed-form optimal solution of $\tau_0$ for given $\{\boldsymbol{\theta}_k\}_{k=0}^{K}$, where the following *theorem* is required,

*Theorem 3:* The optimal solution of $\tau_0$ can be derived in closed form as

$$\tau_0^* = \frac{TB\left\{\exp\left[\mathcal{W}\left(\frac{\frac{C}{B}-1}{\exp(1)}\right)+1\right]-1\right\}}{C + B\left\{\exp\left[\mathcal{W}\left(\frac{\frac{C}{B}-1}{\exp(1)}\right)+1\right]-1\right\}}. \quad (13)$$

*Proof:* See Appendix C. ∎

### B. Optimal Solution of IRS Phase Shifts

In this subsection, we continue to solve problem (11) to derive the optimal solution of the IRS phase shifts, i.e., $\{\boldsymbol{\theta}_k\}_{k=0}^{K}$. It is obvious that solving problem (11) is equivalent to:

$$\max_{\boldsymbol{\theta}_k} \sum_{k=1}^{K} \sum_{q=1}^{Q_k} \frac{X_{k,q} \left|g_{d,k,q} + \boldsymbol{\theta}_0 \mathbf{a}_{k,q}\right|^2 \left|h_{d,k,q} + \boldsymbol{\theta}_k \mathbf{b}_{k,q}\right|^2}{Y_{k,q} \left|g_{d,k,q} + \boldsymbol{\theta}_0 \mathbf{a}_{k,q}\right|^2 + c_{k,q}^2},$$
$$s.t. \ (4a), \quad (14)$$

where $X_{k,q} = (a_{k,q} c_{k,q} - b_{k,q}) P_0$, $Y_{k,q} = c_{k,q} P_0$. As the multiple IRS phase shifts lead to the non-convexity of problem (14), an AO algorithm is proposed to alternately design the IRS beamformers, indicating $\boldsymbol{\theta}_0$ and $\{\boldsymbol{\theta}_k\}_{k=1}^{K}$.

*1) Optimal solution of $\{\boldsymbol{\theta}_k\}_{k=1}^{K}$:* Firstly, we optimize $\{\boldsymbol{\theta}_k\}_{k=1}^{K}$ with a fixed $\boldsymbol{\theta}_0$. Let us denote $D_{k,q} = \frac{X_{k,q} \left|g_{d,k,q} + \boldsymbol{\theta}_0 \mathbf{a}_{k,q}\right|^2}{Y_{k,q} \left|g_{d,k,q} + \boldsymbol{\theta}_0 \mathbf{a}_{k,q}\right|^2 + c_{k,q}^2}$, then problem (14) can be rewritten, with respect to $\{\boldsymbol{\theta}_k\}_{k=1}^{K}$, as

$$\max_{\boldsymbol{\theta}_k} \sum_{q=1}^{Q_k} D_{k,q} \left|h_{d,k,q} + \boldsymbol{\theta}_k \mathbf{b}_{k,q}\right|^2 \quad (15a)$$
$$s.t. \ \left|\theta_{k,n}\right| = 1, \forall n \in [1, N], \ \forall k \in [1, K]. \quad (15b)$$

Let us further expand the objective function (15a), and express it as

$$\sum_{q=1}^{Q_k} D_{k,q} \left|h_{d,k,q} + \boldsymbol{\theta}_k \mathbf{b}_{k,q}\right|^2 = \boldsymbol{\theta}_k \tilde{\boldsymbol{\Delta}}_k \boldsymbol{\theta}_k^H + 2\Re\left\{\boldsymbol{\theta}_k \boldsymbol{\gamma}_k\right\} + d, \quad (16)$$

where $\tilde{\boldsymbol{\Delta}}_k = \sum_{q=1}^{Q_k} D_{k,q} \mathbf{b}_{k,q} \mathbf{b}_{k,q}^H$, $\boldsymbol{\gamma}_k = \sum_{q=1}^{Q_k} D_{k,q} \text{conj}(h_{d,k,q}) \mathbf{b}_{k,q}$, $d = \sum_{q=1}^{Q_k} D_{k,q} h_{d,k,q} \text{conj}(h_{d,k,q})$. Then, problem (15) can be represented as

$$\min_{\boldsymbol{\theta}_k} \boldsymbol{\theta}_k \boldsymbol{\Delta}_k \boldsymbol{\theta}_k^H - 2\Re\left\{\boldsymbol{\theta}_k \boldsymbol{\gamma}_k\right\}, \ s.t. \ (15b) \quad (17)$$

where $\boldsymbol{\Delta}_k = -\tilde{\boldsymbol{\Delta}}_k$. To solve problem (17), the MM and RMO algorithms are proposed below to iteratively optimize $\{\boldsymbol{\theta}_k\}_{k=1}^{K}$ for a given $\boldsymbol{\theta}_0$.

a. **MM Algorithm**: The MM algorithm is adopted here to transform problem (17) into a tractable sequence of form, which utilizes the linear approximation to handle the objective function and constraint of (17), and its approximated solution is iteratively updated in an alternating manner [26]. To apply this algorithm, we first denote $f_{1,k}(\boldsymbol{\theta}_k)$ as the objective function of (17), and then present the following *lemma*,

*Lemma 1:* For the $k$-th cluster at the $m$-th iteration, the objective function $f_{1,k}(\boldsymbol{\theta}_k)$ can be approximated for any given $\boldsymbol{\theta}_k^{(m)}$ [26], [27]. Let $d_k = \boldsymbol{\theta}_k^{(m)} \left(\lambda_{\max}\left(\boldsymbol{\Delta}_k\right) \mathbf{I}_{N \times N} - \boldsymbol{\Delta}_k\right) \left(\boldsymbol{\theta}_k^{(m)}\right)^H$, $\boldsymbol{\Gamma}_k = \lambda_{\max}\left(\boldsymbol{\Delta}_k\right) \mathbf{I}_{N \times N}$; $\lambda_{\max}\left(\boldsymbol{\Delta}_k\right)$ and $\boldsymbol{\theta}_k^{(m)}$ denote the maximum eigenvalue of $\boldsymbol{\Delta}_k$ and the approximated solution

of $\boldsymbol{\theta}_k$ at the $m$-th iteration, respectively. We have

$$\begin{aligned} f_{1,k}(\boldsymbol{\theta}_k) &\triangleq \boldsymbol{\theta}_k \boldsymbol{\Delta}_k \boldsymbol{\theta}_k^H - 2\Re\{\boldsymbol{\theta}_k \boldsymbol{\gamma}_k\} \\ &\leq \boldsymbol{\theta}_k \boldsymbol{\Gamma}_k \boldsymbol{\theta}_k^H - 2\Re\left\{\boldsymbol{\theta}_k \left[(\boldsymbol{\Gamma}_k - \boldsymbol{\Delta}_k)\left(\boldsymbol{\theta}_k^{(m)}\right)^H + \boldsymbol{\gamma}_k\right]\right\} \\ &\quad + \boldsymbol{\theta}_k^{(m)}(\boldsymbol{\Gamma}_k - \boldsymbol{\Delta}_k)\left(\boldsymbol{\theta}_k^{(m)}\right)^H \\ &= \lambda_{\max}(\boldsymbol{\Delta}_k)\|\boldsymbol{\theta}_k\|^2 - 2\Re\{\boldsymbol{\theta}_k[(\lambda_{\max}(\boldsymbol{\Delta}_k)\mathbf{I}_{N\times N} \\ &\quad - \boldsymbol{\Delta}_k)\left(\boldsymbol{\theta}_k^{(m)}\right)^H + \boldsymbol{\gamma}_k]\} + d_k \\ &\triangleq g_{1,k}\left(\boldsymbol{\theta}_k | \boldsymbol{\theta}_k^{(m)}\right), \ \forall k \in [1,K], \end{aligned} \tag{18}$$

As shown in (18), $f_{1,k}(\boldsymbol{\theta}_k)$ is transformed to its surrogate $g_{1,k}\left(\boldsymbol{\theta}_k | \boldsymbol{\theta}_k^{(m)}\right)$, which guarantees the conditions of [27, Eq. 46] and the equivalence of the problem (17) to:

$$\begin{aligned} \min_{\boldsymbol{\theta}_k} \ & \lambda_{\max}\|\boldsymbol{\theta}_k\|^2 - 2\Re\{\boldsymbol{\theta}_k[(\lambda_{\max}(\boldsymbol{\Delta}_k)\mathbf{I}_{N\times N} \\ & - \boldsymbol{\Delta}_k)\left(\boldsymbol{\theta}_k^{(m)}\right)^H + \boldsymbol{\gamma}_k]\}, \ s.t. \ (15b). \end{aligned} \tag{19}$$

In (19), we set $\|\boldsymbol{\theta}_k\|^2 = N$ such that the first term of the objective function is constant. In this case, the optimal solution of $\boldsymbol{\theta}_k$ and $(\lambda_{\max}(\boldsymbol{\Delta}_k)\mathbf{I}_{N\times N} - \boldsymbol{\Delta}_k)\left(\boldsymbol{\theta}_k^{(m)}\right)^H + \boldsymbol{\gamma}_k$ should be identical. Therefore, we have

$$\theta_{k,n}^* = \exp\left(j \arg[\bar{\boldsymbol{\gamma}}_k(n)]\right), \ \forall k \in [1,K], \ \forall n \in [1,N], \tag{20}$$

where $\bar{\boldsymbol{\gamma}}_k = (\lambda_{\max}(\boldsymbol{\Delta}_k)\mathbf{I}_{N\times N} - \boldsymbol{\Delta}_k)\left(\boldsymbol{\theta}_k^{(m)}\right)^H + \boldsymbol{\gamma}_k$. The proposed MM algorithm can be elaborated as in *Algorithm* 1.

*Algorithm 1:* MM algorithm to solve problem (17).

a) **for** $k = 1:1:K$
   i) **Initialization**: the iterative index $m$, and the initialized solution of $\boldsymbol{\theta}_k$, i.e., $\boldsymbol{\theta}_k^{(1)}$.
   ii) **Calculate** $f_{1,k}\left(\boldsymbol{\theta}_k^{(1)}\right)$.
   iii) **Repeat**:
      A) **Compute** $\boldsymbol{\theta}_k^{(m+1)} = \boldsymbol{\theta}_k^* = [\theta_{k,1}, ..., \theta_{k,N}]$ using (20).
      B) **Calculate** $f_{1,k}\left(\boldsymbol{\theta}_k^{(m+1)}\right)$ and **set** $m = m+1$ until convergence is achieved.
b) **end**
c) **Output** the optimal solution of $\boldsymbol{\theta}_k, \ \forall k \in [1,K]$.

b. **RMO Algorithm**: The RMO algorithm can also be adopted for solving problem (17), which mainly relies on the derivation of the gradient descent over the manifold space [28]. To apply this algorithm, we modify (17) to

$$\max_{\boldsymbol{\theta}_k} f_{2,k}(\boldsymbol{\theta}_k) = \boldsymbol{\theta}_k(\boldsymbol{\Delta}_k + \xi_k \mathbf{I}_{N\times N})\boldsymbol{\theta}_k^H - 2\Re\{\boldsymbol{\theta}_k \boldsymbol{\gamma}_k\}, \ s.t. \ (15b), \tag{21}$$

where $\xi_k > 0, \ \forall k \in [1,K]$ is a constant used to control the convergence of the RMO algorithm. Problem (21) can be equivalent to (17) with $\xi_k \boldsymbol{\theta}_k \boldsymbol{\theta}_k^H = \xi_k N$. The unit-modulus constraint (15b) can be denoted by the manifold, which is the product of $N$ complex sets, i.e., $\mathcal{S}_{\boldsymbol{\theta}_k}^N \triangleq \left\{\mathbf{x}_k \in \mathbb{C}^N : |\mathbf{x}_k| = 1, n \in [1,N]\right\}$, where each set is a sub-manifold.

At the $m$-th iteration, we first consider the direction of (21), the opposite of the gradient in the Euclidean space of $f_{2,k}\left(\boldsymbol{\theta}_k^{(m)}\right)$, which can be written as

$$\begin{aligned} -\nabla_{\boldsymbol{\theta}_k} f_{2,k}\left(\boldsymbol{\theta}_k^{(m)}\right) &= -2(\boldsymbol{\Delta}_k + \xi_k \mathbf{I}_{N\times N})\left(\boldsymbol{\theta}_k^{(m)}\right)^H \\ &\quad + 2\boldsymbol{\gamma}_k, \ \forall k \in [1,K]. \end{aligned} \tag{22}$$

Next, we derive the *Riemannian* gradient of $f_{2,k}\left(\boldsymbol{\theta}_k^{(m)}\right)$ for any feasible $\boldsymbol{\theta}_k^{(m)} \in \mathcal{S}_{\boldsymbol{\theta}_k}^N$, which is implemented within the tangent space $\mathcal{T}_{\boldsymbol{\theta}_k^{(m)}}\mathcal{S}_{\boldsymbol{\theta}_k}^N$ [29]. Therefore, the *Riemannian* gradient is given by the steepest descent as

$$\begin{aligned} \mathbf{Grad}_{\mathcal{T}_{\boldsymbol{\theta}_k}\mathcal{S}_{\boldsymbol{\theta}_k}^N}^{(m)} &= -\nabla_{\boldsymbol{\theta}_k} - \Re\left\{\text{conj}(-\nabla_{\boldsymbol{\theta}_k}) \odot \boldsymbol{\theta}_k^{(m)}\right\} \odot \boldsymbol{\theta}_k^{(m)}, \\ &\forall k \in [1,K]. \end{aligned} \tag{23}$$

Then $\boldsymbol{\theta}_k^{(m)}$ is updated in the tangent space $\mathcal{T}_{\boldsymbol{\theta}_k^{(m)}}\mathcal{S}_{\boldsymbol{\theta}_k}^N$ as

$$\tilde{\boldsymbol{\theta}}_k^{(m)} = \boldsymbol{\theta}_k^{(m)} + \varphi_k \mathbf{Grad}_{\mathcal{T}_{\boldsymbol{\theta}_k}\mathcal{S}_{\boldsymbol{\theta}_k}^N}^{(m)}, \ \forall k \in [1,K], \tag{24}$$

where $\varphi_k, \ \forall k \in [1,K]$, denotes a step size. The last step is to perform the normalization operation to map the updated $\tilde{\boldsymbol{\theta}}_k^{(m)}$ into the manifold $\mathcal{S}_{\boldsymbol{\theta}_k}^N$, which is given by

$$\boldsymbol{\theta}_k^{(m+1)} = \tilde{\boldsymbol{\theta}}_k^{(m)} \odot \frac{1}{\tilde{\boldsymbol{\theta}}_k^{(m)}}, \ \forall k \in [1,K]. \tag{25}$$

Note that the above steps can be carried out after determining the parameters $\xi_k$ and $\varphi_k$, which is important for controlling the convergence of the RMO algorithm. The following *lemma* demonstrates the range of these parameters,

*Lemma 2:* The RMO algorithm tends to a non-increasing behaviour until convergence when the parameters $\xi_k$ and $\varphi_k$ satisfy the following relations,

$$\xi_k \geq \frac{N}{8}\lambda_{\max}(\boldsymbol{\Delta}_k) + \|\boldsymbol{\gamma}_k\|_2, \tag{26a}$$

$$0 < \varphi_k < \frac{1}{\lambda_{\max}(\boldsymbol{\Delta}_k + \xi_k \mathbf{I}_{N\times N})}. \tag{26b}$$

*Proof:* See [28]. ■

Based on the above derivations, we elaborate on the procedures of the RMO algorithm as follows.

*Algorithm 2:* RMO algorithm to solve problem (17).

1) **for** $k = 1:1:K$
   a) **Initialization**: the iterative index $m$, and the initialized solution of $\boldsymbol{\theta}_k$, i.e., $\boldsymbol{\theta}_k^{(1)}$.
   b) **Calculate**: $f_{2,k}\left(\boldsymbol{\theta}_k^{(1)}\right)$.
   c) **Determine**: the parameters $\xi_k$ and $\varphi_k$ via (26).
   d) **Repeat**:
      i) **Obtain** the searching direction of (21) as, $-\nabla_{\boldsymbol{\theta}_k} f_{2,k}\left(\boldsymbol{\theta}_k^{(m)}\right)$ via (22).
      ii) **Project** the searching direction onto the tangent space, i.e., $\mathbf{Grad}_{\mathcal{T}_{\boldsymbol{\theta}_k}\mathcal{S}_{\boldsymbol{\theta}_k}^N}^{(m)}$ via (23).
      iii) **Update** $\tilde{\boldsymbol{\theta}}_k^{(m)}$ via (24).
      iv) **Normalize** $\boldsymbol{\theta}_k^{(m+1)}$ via (25).
      v) **Calculate** $f_{1,k}\left(\boldsymbol{\theta}_k^{(m+1)}\right)$ and **set** $m = m+1$ until convergence.
2) **end**
3) **Output** the optimal solution of $\boldsymbol{\theta}_k$. $\forall k \in [1,K]$.

*2) Optimal Solution of $\boldsymbol{\theta}_0$:* In this subsection, we solve problem (14) to obtain the optimal solution of $\boldsymbol{\theta}_0$, taking into account $\{\boldsymbol{\theta}_k\}_{k=1}^K$ obtained in Section III-B1. Let us denote $\tilde{X}_{k,q} = X_{k,q}\left|h_{d,k,q} + \boldsymbol{\theta}_k \mathbf{b}_{k,q}\right|^2$. Then, (14) is reformulated as

$$\max_{\boldsymbol{\theta}_0} \sum_{k=1}^{K}\sum_{q=1}^{Q_k} \frac{\tilde{X}_{k,q}\left|g_{d,k,q} + \boldsymbol{\theta}_0 \mathbf{a}_{k,q}\right|^2}{Y_{k,q}\left|g_{d,k,q} + \boldsymbol{\theta}_0 \mathbf{a}_{k,q}\right|^2 + c_{k,q}^2} \tag{27a}$$

$$s.t.\ \ |\theta_{0,n}| = 1, \forall n \in [1, N]. \tag{27b}$$

Explicitly, problem (27) is a sum of the multiple fractional functions with respect to $\boldsymbol{\theta}_0$, which is a non-convex problem and intractable. To make it tractable, we propose to use the QT method to transform the fractional function into its subtractive counterpart. Then, by introducing an auxiliary variable $\kappa_{k,q},\ \forall k \in [1, K],\ \forall q \in [1, Q_k]$, the objective function (27a) can be equivalently expressed as

$$\begin{aligned}&\tilde{f}\left(\boldsymbol{\theta}_0\right)\\ =&\sum_{k=1}^{K}\sum_{q=1}^{Q_k} 2\left(\tilde{X}_{k,q}\right)^{\frac{1}{2}} \Re\left\{\text{conj}(\kappa_{k,q}) g_{d,k,q} + \text{conj}(\kappa_{k,q})\boldsymbol{\theta}_0 \mathbf{a}_{k,q}\right\}\\ &-\sum_{k=1}^{K}\sum_{q=1}^{Q_k} \left|\kappa_{k,q}\right|^2 \left(Y_{k,q}\left|g_{d,k,q} + \boldsymbol{\theta}_0 \mathbf{a}_{k,q}\right|^2 + c_{k,q}^2\right),\end{aligned} \tag{28}$$

where

$$\kappa_{k,q}^* = \frac{\left(\tilde{X}_{k,q}\right)^{\frac{1}{2}}\left(g_{d,k,q} + \boldsymbol{\theta}_0 \mathbf{a}_{k,q}\right)}{Y_{k,q}\left|g_{d,k,q} + \boldsymbol{\theta}_0 \mathbf{a}_{k,q}\right|^2 + c_{k,q}^2}. \tag{29}$$

Substituting (28) into (27) yields

$$\max_{\boldsymbol{\theta}_0}\ \tilde{f}_0\left(\boldsymbol{\theta}_0\right),\ s.t.\ \text{(27b)}, \tag{30}$$

which can be solved by iteratively optimizing the variables $\boldsymbol{\theta}_0$ and $\kappa_{k,q}$. In each iteration, we first derive the optimal solution of $\boldsymbol{\theta}_0$ for a given $\kappa_{k,q}$, which is then updated using (29) for a given $\boldsymbol{\theta}_0$. Specifically, for a fixed $\kappa_{k,q}$, $\tilde{f}_0\left(\boldsymbol{\theta}_0\right)$ is expanded to transform problem (30) to

$$\max_{\boldsymbol{\theta}_0}\ -\boldsymbol{\theta}_0 \boldsymbol{\Delta}_0 \boldsymbol{\theta}_0^H + 2\Re\left\{\boldsymbol{\theta}_0\left(\boldsymbol{\phi}_1 - \boldsymbol{\phi}_0\right)\right\} + \left(d_1 - d_0\right),\ s.t.\ \text{(27b)}. \tag{31}$$

where $\boldsymbol{\Delta}_0 = \sum_{k=1}^{K}\sum_{q=1}^{Q_k}\left|\kappa_{k,q}\right|^2 Y_{k,q}\mathbf{a}_{k,q}\mathbf{a}_{k,q}^H$, $\boldsymbol{\phi}_0 = \sum_{k=1}^{K}\sum_{q=1}^{Q_k}\left|\kappa_{k,q}\right|^2 Y_{k,q}\text{conj}(g_{d,k,q})\mathbf{a}_{k,q}$, $\boldsymbol{\phi}_1 = \sum_{k=1}^{K}\sum_{q=1}^{Q_k}\left(\tilde{X}_{k,q}\right)^{\frac{1}{2}}\text{conj}(\kappa_{k,q})\mathbf{a}_{k,q}$, $d_0 = \sum_{k=1}^{K}\sum_{q=1}^{Q_k}\left|\kappa_{k,q}\right|^2 Y_{k,q} g_{d,k,q}\text{conj}(g_{d,k,q}) + \sum_{k=1}^{K}\sum_{q=1}^{Q_k}\left|\kappa_{k,q}\right|^2 c_{k,q}^2$, and $d_1 = 2\Re\left\{\sum_{k=1}^{K}\sum_{q=1}^{Q_k}\left(\tilde{X}_{k,q}\right)^{\frac{1}{2}}\text{conj}(\kappa_{k,q}) g_{d,k,q}\right\}$. Furthermore, without loss of generality, (31) can be represented in a simpler form as

$$\min_{\boldsymbol{\theta}_0}\ \boldsymbol{\theta}_0 \boldsymbol{\Delta}_0 \boldsymbol{\theta}_0^H - 2\Re\left\{\boldsymbol{\theta}_0 \boldsymbol{\gamma}_0\right\},\ s.t.\ \text{(27b)}. \tag{32}$$

where $\boldsymbol{\gamma}_0 = \boldsymbol{\phi}_1 - \boldsymbol{\phi}_0$. Now, problem (32) can be iteratively solved in a similar way to *Algorithm* 1 and *Algorithm* 2 as shown in Section III-B1, which is omitted here to conserve space.

### C. Overall Algorithm To Solve Problem (4)

Based on the discussions in Sections III-A and III-B on the design of the transmission time scheduling, the bandwidth allocation, and the IRS phase shifts, the overall algorithm for solving problem (4) can be established, as detailed in *Algorithm* 3. The convergence of *Algorithm* 3 was analyzed in [30], [31], and thus is not repeated here.

*Algorithm 3:* Overall algorithm to solve problem (4).

1) **Initialization**: the iteration index $r$ and initialized solutions of $\boldsymbol{\theta}_k,\ \forall k \in [0, K]$, i.e., $\boldsymbol{\theta}_k^{(1)}$.
2) **Calculate** the objective value of problem (14), i.e., $f_0\left(\boldsymbol{\theta}_0^{(1)}, \boldsymbol{\theta}_1^{(1)}, ..., \boldsymbol{\theta}_K^{(1)}\right)$.
3) **Repeat**: AO algorithm at the $r$-th iteration
   a) **Given** $\boldsymbol{\theta}_0^{(r)}$, **solve** (17) to **calculate** $\boldsymbol{\theta}_k^{(r+1)},\ \forall k \in [1, K]$, by *Algorithm* 1 or *Algorithm* 2.
   b) **Given** $\boldsymbol{\theta}_k^{(r+1)},\ \forall k \in [1, K]$, **update** $\kappa_{k,q}^{(r+1)} = \kappa_{k,q}^*,\ \forall k \in [1, K],\ \forall q \in [1, Q_k]$ via (29).
   c) **Given** $\boldsymbol{\theta}_k^{(r+1)},\ \kappa_{k,q}^{(r+1)},\ \forall k \in [1, K],\ \forall q \in [1, Q_k]$, **solve** (32) to **calculate** $\boldsymbol{\theta}_0^{(r+1)}$ by an algorithm, which is similar to *Algorithm* 1 or *Algorithm* 2.[2]
   d) **Calculate** $f_0\left(\boldsymbol{\theta}_0^{(r+1)}, \boldsymbol{\theta}_1^{(r+1)}, ..., \boldsymbol{\theta}_K^{(r+1)}\right)$ and **set** $r = r + 1$ until convergence.
4) **Output** the optimal IRS phase shifts $\boldsymbol{\theta}_k^*,\ \forall k \in [0, K]$.
5) **Substitute** $\boldsymbol{\theta}_k^*,\ \forall k \in [0, K]$, into (13) to **calculate** the optimal WET time scheduling $\tau_0^*$, which is applied to (12) to **calculate** the optimal WIT time scheduling $\tau_k^*,\ \forall k \in [1, K]$.
6) **Substitute** $\boldsymbol{\theta}_k^*,\ \tau_k^*,\ \forall k \in [0, K]$, into (9) to **calculate** the optimal bandwidth allocation $w_q^*,\ \forall q \in [1, Q_k],\ \forall k \in [1, K]$.

To proceed, we discuss the computational complexity of *Algorithm* 3, which mainly applies to the AO iteration in Step 3, and to the MM or RMO algorithm in *Algorithm* 1 or *Algorithm* 2, and the QT algorithm. On this basis, we further denote the iteration number to guarantee the convergence of the AO, QT, MM, RMO as $I_{AO}$, $I_{QT}$, $I_{MM}$, and $I_{RMO}$, respectively. The complexity of the MM/RMO algorithm can be calculated as $\mathcal{O}\left(N^3 + I_{MM/RMO}N^2\right)$ [32], and the total complexity of *Algorithm* 3 can be given as $\mathcal{O}\left[\left(N^3 + I_{MM/RMO}N^2\right)(K + I_{QT})I_{AO}\right]$.

## IV. A Benchmark Scheme: IRS Selection Scheme

In Section III, we have considered a scenario where all IRSs aid the energy or information reflections during downlink WET or uplink WIT. In this section, we consider a benchmark scheme, namely, the IRS selection scheme, for the comparison of the system design. In this scheme, each IRS can control its "on/off" state to aid the downlink WET and uplink WIT. We assume that there is at most one IRS activated within a time duration $\tau_k,\ \forall k \in [0, K]$, to assist the multi-cluster IoT devices for energy harvesting or the AP for information reception, respectively. To carry out this scheme, we first define a scheduling vector $\boldsymbol{\chi}_k = [\chi_{0,l}, ..., \chi_{K,l}]$, where each element is a binary variable. The $l$-th IRS is active during $\tau_k$ if $\chi_{k,l} = 1$, otherwise inactive. Furthermore, the scheduling variables satisfy $\sum_{l=1}^{L}\chi_{k,l} = 1,\ \chi_{k,l} \in \{0, 1\},\ \forall k \in [0, K]$.

[2]Set $k = 0$ in *Algorithm* 1 or *Algorithm* 2.

We then express the harvested energy at $\mathcal{D}_{k,q}$ during the downlink WET, as

$$E_{k,q}^{nonlinear} = \tau_0 \frac{(a_{k,q}c_{k,q}-b_{k,q})P_0\left|g_{d,k,q}+\sum_{l=1}^{L}\chi_{0,l}\mathbf{g}_{0,l}\boldsymbol{\Theta}_{0,l}\mathbf{g}_{r,l,k,q}\right|^2}{c_{k,q}P_0\tau_0P_0\left|g_{d,k,q}+\sum_{l=1}^{L}\chi_{0,l}\mathbf{g}_{0,l}\boldsymbol{\Theta}_{0,l}\mathbf{g}_{r,l,k,q}\right|^2+c_{k,q}^2}. \quad (33)$$

By contrast, during the uplink WIT, the sum throughput of the $k$-th cluster can be expressed as (34) on the top of the next page, where $\mathbf{a}_{l,k,q} = \text{diag}\left(\mathbf{g}_{0,l}\right)\mathbf{g}_{r,l,k,q}$, and $\mathbf{b}_{l,k,q} = \text{diag}\left(\mathbf{h}_{k,q,l}\right)\mathbf{h}_{r,l}$.

Now, an optimization problem for the benchmark scheme to maximize the sum throughput via jointly design of the IRS phase shifts, the transmission time slots, the bandwidth allocation, as well as the scheduling variable can be stated as

$$\max_{\boldsymbol{\Omega}_{TDMA-FDMA}} \sum_{k=1}^{K} R_k^{TDMA-FDMA},$$
$$s.t.\ (4b),(4c), |\theta_{k,n}| \leq 1, \forall n \in [1,N_l], \forall l \in [1,L], \forall k \in [0,K],$$
$$\sum_{l=1}^{L}\chi_{k,l} \leq 1,\ \chi_{k,l} \in \{0,1\},\ \forall k \in [0,K],\ \forall l \in [1,L],$$
$$\boldsymbol{\Omega}_{TDMA-FDMA} = \left[\left\{\boldsymbol{\Theta}_{k,l}\right\}_{k=0,l=1}^{K,N_l}, \left\{\tau_k\right\}_{k=0}^{K}, \left\{w_q\right\}_{q=1}^{Q_k}, \left\{\chi_{k,l}\right\}_{k=0,l=1}^{K,L}\right]. \quad (35)$$

To solve problem (35), we start with the similar method as discussed in Section III-A to derive the closed-form solutions for the optimal transmission time slots and bandwidth allocation (to conserve space, the details are not repeated here). Following upon this, we derive the optimal solutions of the IRS phase shifts $\boldsymbol{\theta}_{k,l},\ \forall k \in [0,K],\ \forall l \in [1,L]$, and the scheduling variable $\boldsymbol{\chi}_k,\ \forall k \in [0,K]$, by solving the optimization problem (36) on the top of the next page. Problem (36) can be addressed by using the AO algorithm in Section III-C. Specifically, we can optimize $\boldsymbol{\theta}_{k,l}$ and $\chi_{k,l},\ \forall k \in [1,K],\ \forall l \in [1,L]$, first, for the given $\boldsymbol{\theta}_{0,l}$ and $\chi_{0,l},\ \forall l \in [1,L]$, which are then optimized for given $\boldsymbol{\theta}_{k,l}$ and $\chi_{k,l},\ \forall k \in [1,K],\ \forall l \in [1,L]$. Note that the optimal solutions of $\boldsymbol{\theta}_{k,l},\ \forall k \in [0,K],\ \forall l \in [1,L]$ have been derived in Section III-B. Now we have relaxed problems that can be iteratively solved to optimize $\chi_{k,l},\ \forall k \in [0,K],\ \forall l \in [1,L]$.

1) For a given $\chi_{0,l},\ \chi_{k,l},\ \forall k \in [1,K]$, is optimized as

$$\max_{\chi_{k,l}} \sum_{k=1}^{K}\sum_{q=1}^{Q_k}\tilde{D}_{k,q}\sum_{l=1}^{L}\chi_{k,l}\left|h_{d,k,q}+\boldsymbol{\theta}_{k,l}\mathbf{b}_{l,k,q}\right|^2$$
$$s.t.\ \sum_{l=1}^{L}\chi_{k,l}=1, 0 \leq \chi_{k,l} \leq 1, \forall k \in [1,K], \forall l \in [1,L], \quad (37)$$

where $\tilde{D}_{k,q} = \frac{X_{k,q}\left|g_{d,k,q}+\sum_{l=1}^{L}\chi_{0,l}\boldsymbol{\theta}_{0,l}\mathbf{a}_{l,k,q}\right|^2}{Y_{k,q}\left|g_{d,k,q}+\sum_{l=1}^{L}\chi_{0,l}\boldsymbol{\theta}_{0,l}\mathbf{a}_{l,k,q}\right|^2+c_{k,q}^2}$.

2) For the given $\chi_{k,l},\ \forall k \in [1,K]$, $\chi_{0,l}$ is optimized as

$$\min_{\chi_{0,l}} \sum_{l=1}^{L}\chi_{0,l}\tilde{f}_l,$$
$$s.t.\ \sum_{l=1}^{L}\chi_{0,l}=1,\ 0 \leq \chi_{0,l} \leq 1,\ \forall l \in [1,L], \quad (38)$$

where $\tilde{f}_l = \boldsymbol{\theta}_{0,l}\tilde{\boldsymbol{\Sigma}}_{0,l}\boldsymbol{\theta}_{0,l}^H - 2\Re\left\{\boldsymbol{\theta}_{0,l}\tilde{\boldsymbol{\phi}}_l\right\} - \tilde{d}$, $\tilde{\boldsymbol{\Sigma}}_{0,l} = \sum_{k=1}^{K}\sum_{q=1}^{Q_k}\left|\kappa_{k,q}\right|^2 Y_{k,q}\mathbf{a}_{l,k,q}\mathbf{a}_{l,k,q}^H$, $\tilde{\boldsymbol{\phi}}_l = \left(\sum_{k=1}^{K}\sum_{q=1}^{Q_k}\left(\tilde{X}_{k,q}\right)^{\frac{1}{2}}\text{conj}(\kappa_{k,q})\mathbf{a}_{l,k,q}\right) - \left(\sum_{k=1}^{K}\sum_{q=1}^{Q_k}\left|\kappa_{k,q}\right|^2 Y_{k,q}\text{conj}(g_{d,k,q})\mathbf{a}_{l,k,q}\right)$, $\tilde{X}_{k,q} = X_{k,q}\left|h_{d,k,q}+\sum_{l=1}^{L}\chi_{k,l}\boldsymbol{\theta}_{k,l}\mathbf{b}_{l,k,q}\right|^2$, and $\tilde{d} = 2\Re\left\{\sum_{k=1}^{K}\sum_{q=1}^{Q_k}\left(\tilde{X}_{k,q}\right)^{\frac{1}{2}}\text{conj}(\kappa_{k,q})g_{d,k,q}\right\} - \sum_{l=1}^{L}\chi_{0,l}\sum_{k=1}^{K}\sum_{q=1}^{Q_k}\left|\kappa_{k,q}\right|^2 Y_{k,q}g_{d,k,q}\text{conj}(g_{d,k,q}) - \sum_{k=1}^{K}\sum_{q=1}^{Q_k}\left|\kappa_{k,q}\right|^2 c_{k,q}^2$.

It is observed that both problems (37) and (38) are linear programmes (LPs), which can be readily solved by the standard convex optimization [17]. Correspondingly, we have the following *lemma*:

*Lemma 3:* The optimal solutions of the relaxed problems (37) and (38), denoted by $\chi_{k,l},\ \forall k \in [0,K],\ \forall l \in [1,L]$ guarantee their binary nature.

*Proof:* See [33]. ■

Here we also discuss the computational complexity of the benchmark scheme. Following the similar discussion as for *Algorithm* 3, the benchmark scheme uses the LP to solve problem (37) and problem (38), and the complexity of which can be calculated as $\mathcal{O}\left(KQL\right)$ and $\mathcal{O}\left(L\right)$, respectively. Thus, the total computational complexity of the benchmark scheme is given by

$$\mathcal{O}\left\{\left[\left(N_{l^*}^3+I_{MM/RMO}N_{l^*}^2\right)\left(K+I_{QT}\right)+L(Q*K+I_{QT})\right]I_{AO}\right\}, \quad (39)$$

where $l^*$ denotes the index of the activated IRS.

## V. Numerical Results

This section demonstrates the numerical results to validate the proposed schemes, verify the theoretical derivations, and show the achievable performance. We use a three-dimensional (3-D) coordinate system to describe the network deployment as shown in Fig. 3. In detail, the coordinates of the PS and AP are $(X_{PS}=-10, Y_{PS}=0, Z_{PS}=0)$ and $(X_{AP}=10, Y_{AP}=0, Z_{AP}=0)$, and those of the $l$-th IRS and of $\mathcal{D}_{k,q},\ \forall q \in [1,Q_k],\ \forall k \in [1,K]$, are $(X_{IRS}=X_{IRS,l}=-2, Y_{IRS}=Y_{IRS,l}=6, Z_{IRS,l})$ and $(X_{U,k,q}, Y_{U,k,q}=0, Z_{U,k,q})$, respectively. The $z$-coordinates of IRSs are $Z_{IRS,l}=\frac{x*y}{2}$ for $x=1,....,2*l+1$, and $Z_{IRS,l}=-\frac{(x-1)*y}{2}$ for $x=2,...,2*l$, where $y=4$ is the interval between two neighbouring IRSs. In addition, $\mathcal{D}_{k,q},\ \forall q \in [1,Q_k],\ \forall k \in [1,K]$, is randomly deployed within a circular area in the $x-z$ plane with the centre of $(0, C_{U,k})$ and the radius of 6 m. We set $C_{U,k}=\frac{x*\tilde{y}}{2}$ for $x=1,...,2*k+1$, and $C_{U,k}=-\frac{(x-1)*\tilde{y}}{2}$ for $x=2,...,2*k$, where $\tilde{y}=5$ suggests the distance between two neighbouring clusters. We assume that the channel coefficients are composed of the small-scale fading and the distance-dependent path loss components. Specifically, the channels for the IRS-related links, e.g., $\mathbf{g}_{0,l}$, $g_{r,l,k,q}$, $h_{k,q,l}$, and $h_{r,l}$, are modelled as the Racian fading, while those for the direct links, e.g., $g_{d,k}$ and $h_{d,k}$, are modelled as Rayleigh fading [13]. Moreover, the path loss is denoted by $\mathcal{PL}=A*d_{\omega}^{-\epsilon_{\omega}}$, where $\epsilon_{\omega}$ and $d_{\omega}$ are the

$$R_k = \tau_k \sum_{q=1}^{Q_k} w_q \log\left(1 + \frac{\tau_0 X_{k,q}\left|g_{d,k,q} + \sum_{l=1}^{L}\chi_{0,l}\boldsymbol{\theta}_{0,l}\mathbf{a}_{l,k,q}\right|^2\left|h_{d,k,q} + \sum_{l=1}^{L}\chi_{k,l}\boldsymbol{\theta}_{k,l}\mathbf{b}_{l,k,q}\right|^2}{\tau_k\left(Y_{k,q}\left|g_{d,k,q} + \sum_{l=1}^{L}\chi_{0,l}\boldsymbol{\theta}_{0,l}\mathbf{a}_{l,k,q}\right|^2 + c_{k,q}^2\right)\sigma^2 w_q}\right), \tag{34}$$

$$\max_{\boldsymbol{\theta}_k,\chi_{k,l}} \sum_{k=1}^{K}\sum_{q=1}^{Q_k} \frac{X_{k,q}\left|g_{d,k,q} + \sum_{l=1}^{L}\chi_{0,l}\boldsymbol{\theta}_{0,l}\mathbf{a}_{l,k,q}\right|^2\left|h_{d,k,q} + \sum_{l=1}^{L}\chi_{k,l}\boldsymbol{\theta}_{k,l}\mathbf{b}_{l,k,q}\right|^2}{Y_{k,q}\left|g_{d,k,q} + \sum_{l=1}^{L}\chi_{0,l}\boldsymbol{\theta}_{0,l}\mathbf{a}_{l,k,q}\right|^2 + c_{k,q}^2}$$

$$s.t.\ \ |\theta_{k,n}| = 1,\ \ \sum_{l=1}^{L}\chi_{k,l} = 1,\ \ \chi_{k,l} \in \{0,1\},\ \ \forall n \in [1, N_l],\ \ \forall l \in [1, L],\ \ \forall k \in [0, K]. \tag{36}$$

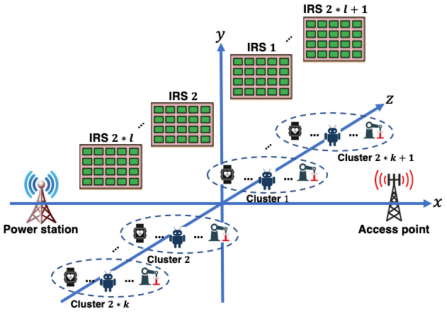


Fig. 3: Network deployment.

path loss exponents and the physical distance between PS and IRS ($\omega = PS2IRS$), or IRS and IoT devices ($\omega = IRS2D$), or IRS and AP ($\omega = IRS2AP$), or PS and IoT devices ($\omega = PS2D$), or IoT devices and AP ($\omega = D2AP$). We consider two different configurations for the numbers of IRS elements and IoT devices, be they **Case 1** and **Case 2**[3]. Unless stated otherwise, the relevant simulation parameters for these two cases are summarized in Table III. Also, in this work, a comprehensive comparison between the proposed scheme and several benchmark schemes is provided, where:

1) *All IRSs' participation*: All IRSs participate in the downlink WET and uplink WIT.
   a) *Proposed scheme*: The MM and RMO algorithms are used in Section III to optimally design the IRS phase shifts and allocate the optimal bandwidth and transmission time. They are denoted by "All IRSs MM" and "All IRSs RMO", respectively.
   b) *Discrete phase shifts (DPS)* [34]: In this case, the discrete phase shift set, i.e., $\mathcal{S}_{\boldsymbol{\theta}_k} = \left\{\theta_{k,n} = \exp\left(j\alpha_{k,n}\right), \alpha_{k,n} \in \left\{0, \frac{2\pi}{L}, ..., \frac{2\pi(L-1)}{L}\right\}\right\}, \forall k \in [0, K], n \in [1, N]$, is introduced to quantize the optimal IRS phase shifts, where $L = 2^{b_0}$ represents the total number of discrete phase shifts, and $b_0$ is the number of bits used for the quantization (typically $b_0 = 1$). These cases are denoted by "All IRSs DPS MM" and "All IRSs DPS RMO".
   c) *Random phase shifts (RPS)*: The phase shifts are randomly chosen from $[0, 2\pi]$, which is denoted by "All IRSs RPS".
   d) *Equal bandwidth and time allocations (EBTA)*: All bandwidth and transmission time slots are equally allocated to $w_q = \frac{B}{Q_k},\ \forall q \in [1, Q_k],\ \forall k \in [1, K]$ and $\tau_k = \frac{T}{1+K},\ \forall k \in [0, K]$. The corresponding scheme is denoted by "All IRSs EBTA".
   e) *Linear energy harvesting (LEH)* [13]: The linear energy harvesting (LEH) model is assumed for all IoT devices during the downlink WET, denoted by "All IRSs LEH".
2) *IRS selection scheme*: At most one IRS participates in the downlink WET or uplink WIT in each cluster. The IRS phase shifts, the bandwidth and transmission time allocations are optimized as in Section III, while the scheduling vector is optimized as that in Section IV. The schemes are denoted by "IRS Selection MM" and "IRS Selection RMO", respectively.
3) *IRS selection with RPS*: At most one IRS participates in the downlink WET or uplink WIT in each cluster. The IRS phase shifts are random values in $[0, 2\pi]$. The scheme is denoted by "IRS Selection RPS".
4) *No IRS*: No IRS participates in the downlink WET and uplink WIT. The bandwidth and transmission time allocations are optimized as the approaches in Section III. The corresponding case is denoted by "WO IRS".
5) *Imperfect CSI*: We consider that the cascaded CSIs, i.e., $\mathbf{a}_{k,q}$ and $\mathbf{b}_{k,q}$, $\forall k \in [1, K]$, $\forall q \in [1, Q_k]$, are not perfectly available and expressed as $\mathbf{a}_{k,q} = \tilde{\mathbf{a}}_{k,q} + \mathbf{e}_{a,k,q}$, and $\mathbf{b}_{k,q} = \tilde{\mathbf{b}}_{k,q} + \mathbf{e}_{b,k,q}$, where $\tilde{\mathbf{a}}_{k,q}$ and $\tilde{\mathbf{b}}_{k,q}$ are the estimated cascaded channels; $\mathbf{e}_{a,k,q}$ and $\mathbf{e}_{b,k,q}$ are the corresponding estimation errors with Gaussian entries, i.e., with independent and identically distributed (i.i.d.) zero mean and variances $\delta_{e,a}$ and $\delta_{e,a}$, respectively. For simplicity and without loss of generality, we set the cascade CSI error factors as $\delta_{e,a} = \delta_{e,b} = \delta_e$.

[3]**Case 1** considers different numbers of IRS elements and IoT devices at each cluster, which can be treated as a case with a random deployment of the numbers of the IRS elements and IoT devices; **Case 2** considers the same numbers of IRS elements and IoT devices at each cluster, which facilitates the system configuration to simulate the sum throughput versus these parameters.

### A. Impact of Transmit Power of PS

In this subsection, we examine the impact of the transmit power $P_0$ of the PS on the sum throughput, energy time scheduling, and average harvested energy of all IoT devices for both cases. The results are shown in Figs. 4 - 9. We first discuss the simulation results under the configuration of **Case 1**. In Fig. 4, the sum throughput shows a monotonically increasing

TABLE III: **Notations of Simulation Parameters**

| Parameters & Values | Parameters & Values | Parameters & Values | Parameters & Values |
|---|---|---|---|
| $P_0 = 30$ dBm or 1 W | $K = 4$ | $L = 5$ | $T = 1$ second |
| $B = 1$ | $\sigma^2 = -170$ dBm/Hz | **Case 1**: $N_l = [10, 20, 25, 15, 30]$, $Q_k = [4, 5, 5, 6]$ | **Case 2**: $N_l = [30, 30, 30, 30, 30]$, $Q_k = [10, 10, 10, 10]$ |
| $\epsilon_{PS2RIS} = \epsilon_{RIS2AP} = 2$ | $\epsilon_{RIS2D} = 2.5$ | $\epsilon_{PS2D} = \epsilon_{D2AP} = 3.5$ | $A = 10^{-2}$ |

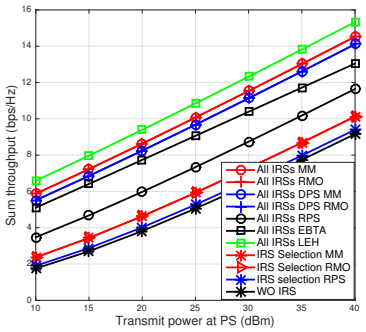


Fig. 4: Sum throughput versus transmit power at PS.

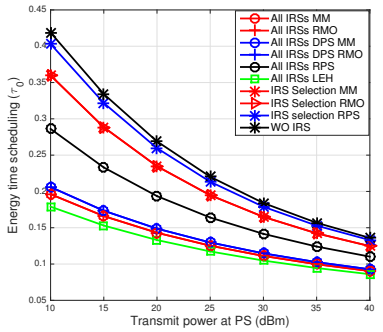


Fig. 5: Energy time scheduling versus transmit power at PS.

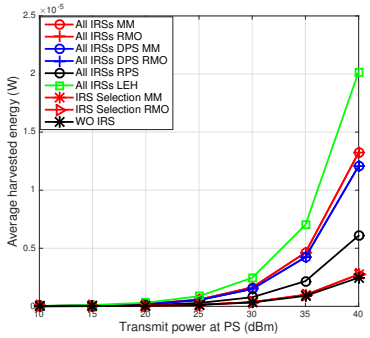


Fig. 6: Average harvested energy versus transmit power at PS.

trend with respect to $P_0$ for all schemes. Specifically, the proposed schemes with the MM and RMO algorithms provide very similar results, which verifies the effectiveness of the proposed algorithms. Also, the proposed schemes with MM and RMO algorithms outperform their DPS counterparts, due to the fact that the quantized phase shifts can incur the imperfect alignment for the optimal phase shifts of downlink WET and uplink WIT, and therefore, degrading the sum throughput performance. In addition, the proposed schemes demonstrate a significantly better performance than the schemes with RPS and with EBTA, which confirms the optimal IRS phase shift design as well as the optimal time scheduling and bandwidth allocation of our proposed schemes. Moreover, the proposed schemes significantly outperform the IRS selection schemes, which can be explained by the fact that in the proposed schemes, all IRSs participate the energy harvesting and data transmission. By constrast, in the IRS selection schemes, only one IRS is used to improve energy/information reflection in each time period. However, both the proposed and the IRS selection schemes outperform the schemes without IRSs, which highlights the benefits induced by the IRS. Furthermore, the LEH scheme provides an upper bound performance for the proposed schemes in terms of the sum throughput, which is originated from that the energy conversion efficiency $\eta$ of the LEH model leads to an ideal case that outperforms the NLEH model in the proposed schemes.

Fig. 5 and Fig. 6 show the energy time scheduling $\tau_0$ and the average harvested energy versus $P_0$, respectively. Specifically, for all schemes, the optimal energy time scheduling decreases with the increase of $P_0$. The gap between the proposed schemes and the other benchmark schemes becomes smaller as $P_0$ increases. While the average harvested energy increases with respect to $P_0$, the gap between the proposed schemes and the other benchmark schemes becomes larger as $P_0$ increases. Fig. 5 shows that the proposed schemes consume less time for downlink WET than the schemes with DPS, the scheme with RPS, the IRS selection schemes, the IRS selection scheme with RPS and that without IRSs, respectively. Therefore, the proposed schemes can provide an energy saving at the PS, which is beneficial, as more time duration can be assigned to the IoT devices for uplink WIT so as to enhance the throughput performance. In addition, the LEH scheme provides a lower bound for the proposed schemes in terms of the energy time scheduling, since the energy conversion efficiency $\eta$ of the LEH model induces an ideal case, yielding less time for the downlink WET than the NLEH model.

Fig. 6 illustrates that the average harvested energy of all IoT devices monotonically increases in terms of $P_0$, which reveals that the decline of $\tau_0$ may not at a cost of the harvested energy for the IoT devices for all schemes. Again, the proposed schemes outperform that with DPS, that with RPS, and that without IRSs. This can be explained as the energy reflection at the IoT devices effectively improved via the employment of IRS and the optimal design of the phase shifts. Moreover, the IRS selection schemes harvest much less energy than the proposed schemes, and collect more energy than the scheme without IRSs, respectively. In addition, the LEH scheme offers an upper bound for the proposed schemes in terms of the average harvested energy, again due to the the idealized energy conversion efficiency $\eta$. The simulation results under the configurations of **Case 2** are shown in Figs. 7 - 9. The observations and corresponding arguments for these numerical results are the same as that of **Case 1**, which are omitted here.

### *B. Impact of IRS Deployment*

In this subsection, we examine the impact of IRS deployment on the sum throughput, energy time scheduling, and average harvested energy of all IoT devices for both considered cases. These results are demonstrated in Figs. 10 - 15. First, let us explain the numerical results under the configuration of **Case 1**. In detail, Fig. 10 shows the sum throughput versus the x-coordinate $X_{IRS}$ of IRS, exhibiting that the sum throughput of all IRS-related schemes first increases and then decline with respect to $X_{IRS}$. Therefore, there are optimum

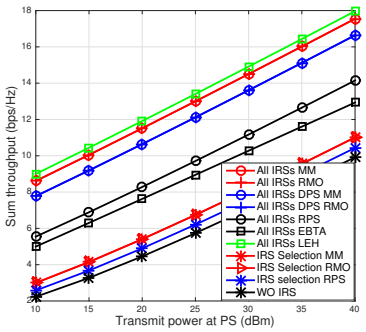


Fig. 7: Sum throughput versus transmit power at PS.

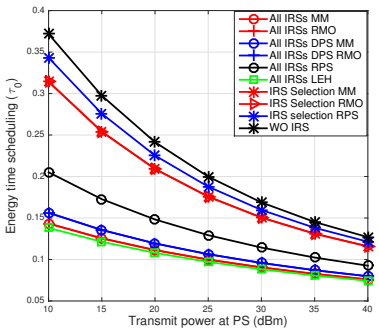


Fig. 8: Energy time scheduling versus transmit power at PS.

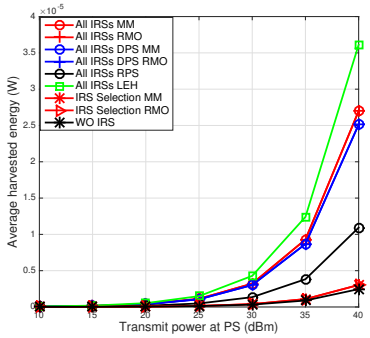


Fig. 9: Average harvested energy versus transmit power at PS.

IRSs' locations to achieve the maximum sum throughput performance. The results show that the proposed schemes (i.e., MM and RMO) outperforms their DPS counterparts, the scheme with RPS, the scheme with EBTA, the IRS selection schemes (i.e., MM and RMO), the IRS selection scheme with RPS, as well as the scheme without IRSs (remaining constant with respect to $X_{IRS}$). The reasons of the observations can be explained by the facts: 1) The employment of IRS is beneficial to performance improvement; 2) the quantized phase shifts induce the mismatch to the real ones leading to a performance loss; 3) the proposed schemes benefit from the optimal IRS phase shift design as well as the optimal time scheduling and bandwidth allocation; 4) the IRS selection schemes only use one of the IRSs for energy/information reflection in each time period, instead of using all IRSs in the proposed schemes. As shown in Fig. 10, the LEH scheme provides an upper bound for the proposed schemes by appealing an ideal energy conversion efficiency $\eta$.

Fig. 11 illustrates the energy time scheduling $\tau_0$ versus $X_{IRS}$, where all the IRS related schemes first exhibit a decreasing trend and then increase with $X_{IRS}$. Explicitly, the proposed schemes require less time for the downlink WET than the schemes with DPS, the scheme with RPS, the IRS selection schemes, the IRS selection scheme with RPS and the scheme without IRSs. Hence, it can save more energy of the PS and provide more time for the IoT devices to carry out the uplink WIT, which hence enhances the throughput performance. Again, the LEH scheme provides a lower bound for the proposed schemes, since that an ideal $\eta$ applied.

In Fig. 12, we show the average harvested energy versus $X_{IRS}$. The result shows that the harvested energy by all the IRS related schemes first increases and then decreases with $X_{IRS}$, illustrating the optimal IRS deployment exists in practice. The proposed schemes outperforms the schemes with DPS, the scheme with RPS and the scheme without IRSs (remaining constant with $X_{IRS}$). Thus, the energy harvesting capability of the IoT devices can be effectively improved by the optimal design of the phase shifts and the aid of IRSs. Moreover, the IRS selection schemes significantly harvest less energy than the proposed schemes with all IRSs' participation, and collect more energy than the scheme without IRSs, respectively. Again, the LEH model assuming the ideal energy conversion efficiency $\eta$ induces perfect energy harvesting, yielding the upper bound performance. The simulation results under the configuration of **Case 2** are shown in Figs. 13 - 15, which provide similar observations as Figs. 10 - 12. The corresponding discussion and explanation are also very similar as that in **Case 1**. Thus, the details are omitted.

### *C. Impact of Number of IRSs/Reflecting Elements of Each IRS*

This subsection illustrates the impact of the number of reflecting elements of each IRS and the number of IRSs on the sum throughput, the energy time scheduling, and the average harvested energy in **Case 2**. First, we investigate the sum throughput, the energy time scheduling, and the average harvested energy versus the number of reflecting elements of each IRS (i.e., $N_0 = N_l,\ \forall l = \{1, ..., L\}$) in Figs. 16 - 18. In details, as shown in Fig. 16, all the IRS related schemes have a monotonically increased throughput as $N_0$ increases. The proposed schemes outperform their own DPS version's scheme, and also outperform the scheme with RPS, the scheme with EBTA, the IRS selection schemes, the IRS selection scheme with RPS, and the scheme without IRSs (remaining constant with $N_0$). Therefore, the employment of IRSs, the optimal design of the IRS phase shifts, the optimal time scheduling and bandwidth allocation, are important for performance improvement. As seen in Fig. 16, the LEH scheme achieves a better throughput performance than the proposed schemes, owing to the assumption of an ideal $\eta$.

From Fig. 17, we observe that the energy time scheduling $\tau_0$ demonstrates a monotonically decreasing behaviour with the number of reflecting elements per IRS for all the IRS related schemes. As expected, the proposed schemes consume less time for downlink WET than their DPS relied schemes, and also than the scheme with RPS, the IRS selection scheme, the IRS selection scheme with RPS, and the scheme without IRSs (remaining constant with $N_0$), which is even more time consuming than the LEH scheme.

Fig. 18 shows that the average harvested energy increases with respect to $N_0$ for all the IRS related schemes. Again, the proposed schemes outperform the other benchmark schemes, including, the schemes with DPS, the scheme with RPS, the IRS selection schemes, and the scheme without IRSs.

The impact of the number of IRS $L$ on the sum throughput, the energy time scheduling, and the average harvested energy is shown in Figs. 19 - 21, respectively. The observations are and explanations of these numerical results are same as for Figs. 16 - 18. Hence, the details are omitted here for brevity.

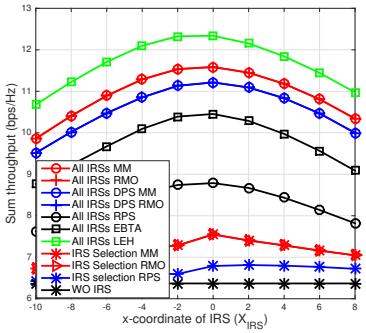


Fig. 10: Sum throughput versus x-coordinate of IRSs.

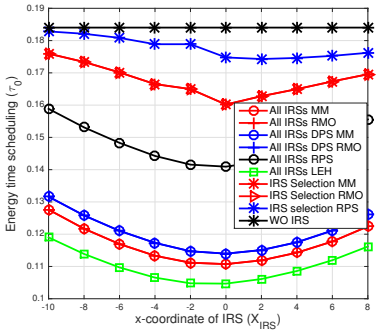


Fig. 11: Energy time scheduling versus x-coordinate of IRSs.

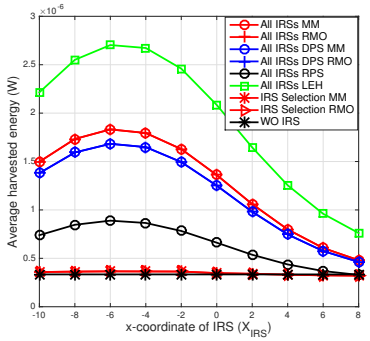


Fig. 12: Average harvested energy versus x-coordinate of IRSs.

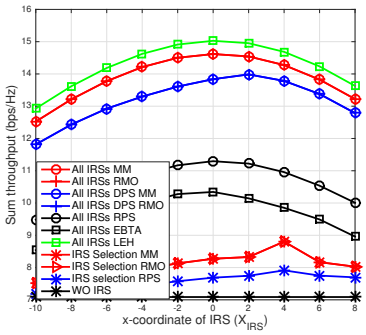


Fig. 13: Sum throughput versus x-coordinate of IRSs.

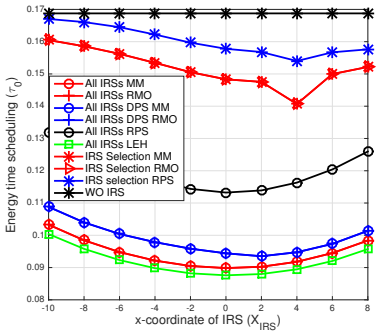


Fig. 14: Energy time scheduling versus x-coordinate of IRSs.

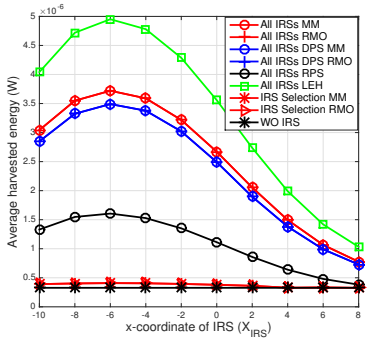


Fig. 15: Average harvested energy versus x-coordinate of IRSs.

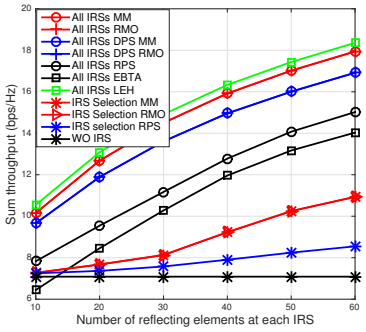


Fig. 16: Sum throughput versus number of reflecting elements at each IRS.

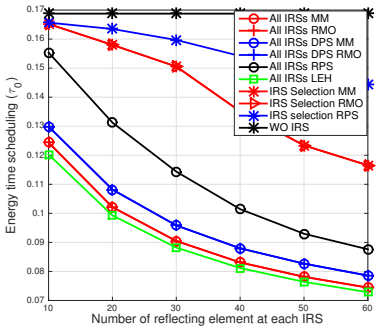


Fig. 17: Energy time scheduling versus number of reflecting elements at each IRS.

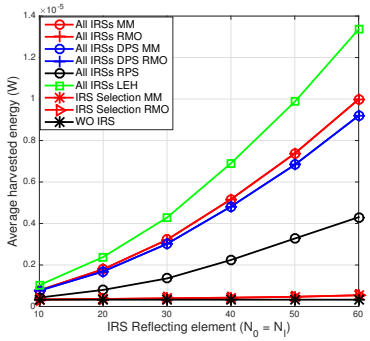


Fig. 18: Average harvested energy versus number of reflecting elements at each IRS.

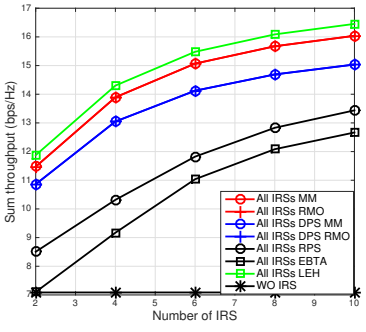


Fig. 19: Sum throughput versus number of IRSs.

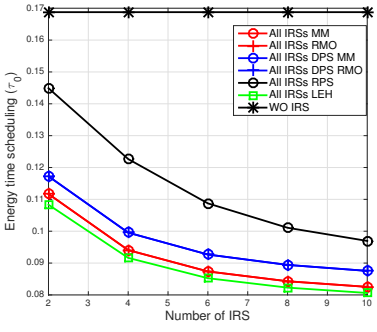


Fig. 20: Energy time scheduling versus number of IRSs.

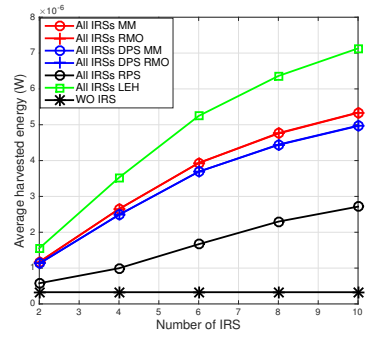


Fig. 21: Average harvested energy versus number of IRSs.

### D. Impact of Number of Clusters/IoT Devices of Each Cluster

Fig. 22 demonstrates the sum throughput versus the number of clusters $K$ for all considered schemes. As $K$ increases, the sum throughput exhibits an monotonically increasing trend, and this increase gain approaches to a flat in the larger cluster region. This is because, as $K$ increases, more clusters may be located farther away from the PS, and the AP, which reduces the energy harvesting efficiency of the IoT devices and therefore, degrades the information reception at the AP. Fig. 23 shows that the sum throughput achieved by all the schemes monotonically increases with respect to the number of IoT devices per cluster. It can be seen that similar insights as from Fig. 22 can be gained from Fig. 23.

### E. Impact of Number of Bits

Fig. 24 demonstrates the sum throughput performance versus the number of bits $b_0$ for the quantization, with respect to different configurations of clusters. It can be readily seen from the result that the performance gap between the optimal phase shifts and the quantized phase shifts gradually decreases when $b_0$ increases from 1 bit to 6 bits. This is because the phase alignment errors resulted from the quantizations become smaller, as $b_0$ increases. Hence, the performance loss becomes smaller and approaches the performance of its continuous counterpart, as $b_0$ increases. In addition, a larger $b_0$ yields a higher granularity of phase shifts to be selected for energy and information reflections, which approaches the continuous counterpart in terms of the sum throughput.

### F. Comparison between Perfect and Imperfect CSI

Finally, we provide the comparison between the proposed/benchmark scheme with perfect and imperfect CSI cases in Fig. 25 and Fig. 26. In Fig. 25, the sum throughput performance is demonstrated against $P_0$ with $N_0 = 30,$ or 60. As indicated by the result, there is a clear performance degradation in the imperfect CSI case compared to the perfect case. The impact of the CSI estimation error $\delta_e$ on the sum throughput is examined in Fig. 26, and the result shows a severely declining sum throughput performance with respect to $\delta_e$.

## VI. Conclusions

This paper investigated a multi-IRS assisted multi-cluster WP-IoT network, where IoT devices employ the fractional NLEH model to harvest energy for their information transmission with the aid of multiple IRSs. The system was designed to maximize sum throughput by jointly optimizing the IRS phase shifts, the transmission time scheduling, and the bandwidth allocation. By exploiting the Lagrange dual method and the KKT conditions, the transmission time scheduling and bandwidth allocation were derived in closed-forms. Furthermore, the QT was applied to transform the sum of multiple fractional programming to the subtractive form, in which the MM and RMO methods were proposed to iteratively derive the closed-form IRS phase shifts for downlink WET and uplink WIT. Moreover, an IRS selection scheme was introduced to facilitate the system design, where each of the IRSs can control its "on/off" state to flexibly participate the downlink WET and uplink WIT to allow at most one IRS to be activated within a time slot. Numerical results verified the optimality of the proposed schemes, and confirmed the benefits induced by the IRS to coordinate the relations among sum throughput, energy time scheduling, and average harvested energy.

For future work, we will consider the IRS-assisted WP IoT networks with multi-antenna PS and AP, where the active energy beamforming, the passive IRS beam patterns of downlink WET and uplink WIT, the received decoding beamforming for each device, and the transmission time scheduling can be optimized in an alternated manner. Also, the AP can utilize the multi-device decomposition (MUD) technique to recover each device's signal. Other promising topic areas that are worth investigating include: the impact of imperfect cascaded CSI on the network throughput, where robust optimization can be exploited based on the modelling of channel estimation errors, e.g., bounded or statistical quantity; the IRS-aided WP-IoT network with channel coherence block, where multi-transmission-block case may require to frequently update the optimal IRS beam patterns by solving the throughput maximization problem for each transmission block; the WET at IRS with alternating current (AC) for IRS controller computation, where the RF energy radiated by the PS in downlink WET is divided into three portions: the direct current (DC) harvested power dedicated for the circuit operation of the IRS controller, the AC signal power dedicated for supplying the AC computational logic of the IRS controller, and the IRS passively reflects energy from PS to IoT devices; the hybrid TDMA-NOMA scheme, where different groups of IoT devices delivery information at their dedicated time slots via TDMA, while all devices in each group concurrently transmit information via NOMA; the spatial-division multiple access (SDMA) in the IRS assisted WP IoT network when the AP is equipped with multiple antenna, where all IoT devices simultaneously deliver their information resulting in interference. Moreover, one may consider to apply the IRS to WP-mobile edge computing or WP-wireless caching to effectively reap the benefits of computational latency and energy consumption.

## Appendix

### A. Proof of Theorem 1

To prove *Theorem* 1, we first consider the Lagrange dual function of (6), which is

$$\mathcal{L}_1\left(w_q,\lambda\right)=\sum_{q=1}^{Q_k} w_q \log\left(1+\frac{A_{k,q}}{w_q}\right)-\lambda\left(\sum_{q=1}^{Q_k} w_q - B\right). \tag{40}$$

By setting its first-order derivative to zero, i.e.,

$$\frac{\partial \mathcal{L}_1}{\partial w_q}=0 \Rightarrow \log\left(1+\frac{A_{k,q}}{w_q}\right)-\frac{\frac{A_{k,q}}{w_q}}{1+\frac{A_{k,q}}{w_q}}-\lambda=0, \tag{41}$$

and after some mathematical manipulations, we obtain the optimal solution of $w_q$ in (9). Substituting it into problem (6) gives (8). This completes the proof of *Theorem* 1.

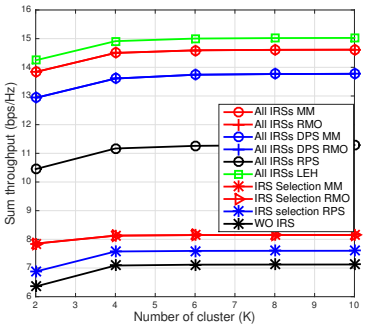


Fig. 22: Sum throughput versus number of clusters.

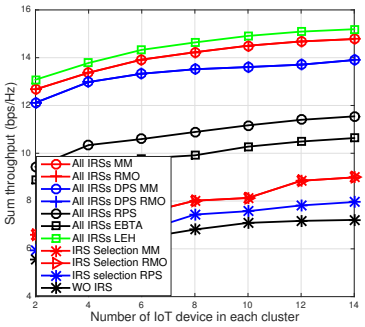


Fig. 23: Sum throughput vs number of IoT devices in each cluster.

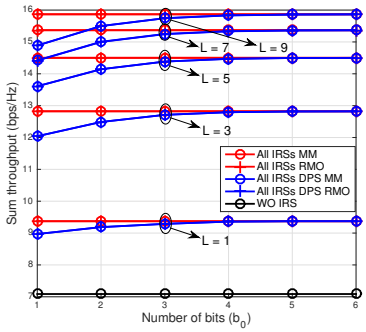


Fig. 24: Sum throughput versus number of quantized bits $b_0$.

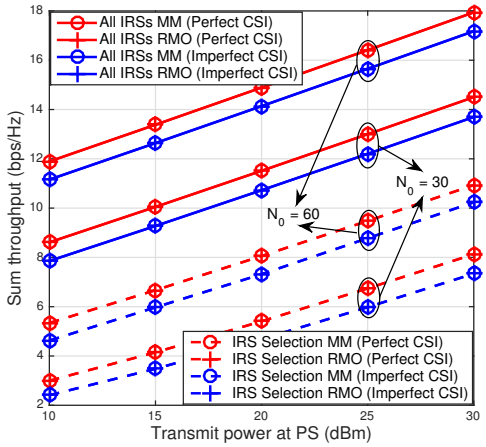


Fig. 25: Sum throughput with im-/perfect CSI.

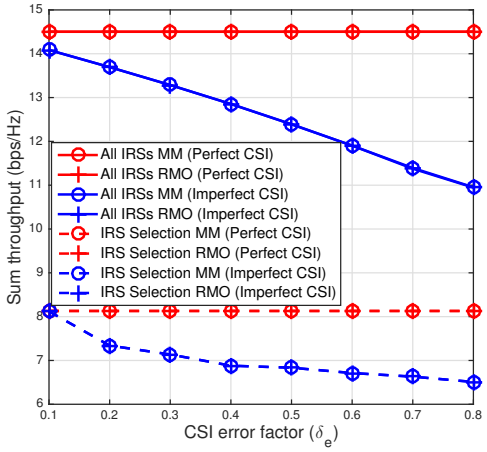


Fig. 26: Sum throughput versus CSI error factor $\delta_e$.

### B. *Proof of* Theorem 2

To prove *Theorem* 2, we first write the Lagrange dual function of (10) as

$$\mathcal{L}_2\left(\tau_0,\{\tau_k\}_{k=1}^K,\mu\right) = \sum_{k=1}^K \tau_k B\log\left(1+\frac{\tau_0\sum_{q=1}^{Q_k}C_{k,q}}{\tau_k B\sigma^2}\right) - \mu\left(\sum_{k=0}^K\tau_k - T\right), \tag{42}$$

where $\mu$ is the non-negative dual variable with the time scheduling constraint (4b). Also, the associated dual problem is given by

$$\min_{\{\tau_0,\{\tau_k\}_{k=1}^K\}\in\mathcal{S}} \mathcal{L}_2\left(\tau_0,\{\tau_k\}_{k=1}^K,\mu\right), \tag{43}$$

where $\mathcal{S}$ represents the feasible set with $\{\tau_k\}_{k=0}^K \in [0,1]$, as shown by constraint (4b). For given $\{\boldsymbol{\theta}_k\}_{k=0}^K$, (10) is a convex problem with $\{\tau_k\}_{k=0}^K$ satisfying the feasible set $\mathcal{S}$. Hence, the optimal solution obtained from (10), denoted by $\{\bar{\tau}_k\}_{k=0}^K$, is equivalent to that obtained from its dual problem (43), denoted by $\{\hat{\tau}_k\}_{k=0}^K$, such that the objective values of (10) and (43) are identical. Hence, the dual problem (43) guarantees the Slater's condition, and strong duality between (10) and (43) always holds. Correspondingly, the following KKT conditions are satisfied for the optimal solution of (10), denoted by $\{\tau_k^*\}_{k=0}^K$, which is given as

$$\mu^*\left(\tau_0^*+\sum_{k=1}^K\tau_k^*-T\right)=0, \tag{44a}$$

$$\frac{\partial\mathcal{L}_2}{\partial\tau_k}=0,\ \forall k\in[1,K]. \tag{44b}$$

From (44a), it is easily verified that $\mu^*>0$ holds to guarantee $\sum_{k=0}^K\tau_k^*=T$. Next, from (44b), we have

$$\frac{\partial\mathcal{L}_2}{\partial\tau_k}=B\left[\log\left(1+\frac{\tau_0\sum_{q=1}^{Q_k}C_{k,q}}{\tau_k B\sigma^2}\right)-\frac{\frac{\tau_0\sum_{q=1}^{Q_k}C_{k,q}}{\tau_k B\sigma^2}}{1+\frac{\tau_0\sum_{q=1}^{Q_k}C_{k,q}}{\tau_k B\sigma^2}}\right]-\mu=0, \tag{45}$$

which takes the form of $f(z)=\log(1+z)-\frac{z}{1+z}$, meaning that is a monotonically increasing function of $z$. Therefore, the following $K$ equations are satisfied,

$$\frac{\tau_0\sum_{q=1}^{Q_1}C_{1,q}}{\tau_1 B\sigma^2}=,\ldots,=\frac{\tau_0\sum_{q=1}^{Q_K}C_{K,q}}{\tau_K B\sigma^2}. \tag{46}$$

Let us denote as $\rho^{-1}=\frac{\tau_0\sum_{q=1}^{Q_k}C_{k,q}}{\tau_k B\sigma^2}$, thus $\tau_k$ is derived as

$$\tau_k=\frac{\rho\tau_0\sum_{q=1}^{Q_k}C_{k,q}}{B\sigma^2}. \tag{47}$$

Then, using $\sum_{k=0}^K\tau_k=T$, $\rho$ can be derived as,

$$\rho=\frac{(T-\tau_0)B\sigma^2}{\tau_0\sum_{k=1}^K\sum_{q=1}^{Q_k}C_{k,q}}. \tag{48}$$

Finally, upon substituting (48) into (47), we obtain the optimal solution of $\tau_k$ as shown in (12), which is further plugged

into problem (10) to obtain its equivalent form of (11). This completes the proof of *Theorem* 2.

### C. *Proof of* Theorem *3*

Let us define $C = \frac{\sum_{k=1}^{K}\sum_{q=1}^{Q_k} C_{k,q}}{\sigma^2}$. Then, after calculating the first-order derivative of $f_0\left(\{\boldsymbol{\theta}_k\}_{k=0}^{K}, \tau_0\right)$ with respect to $\tau_0$, and setting the result to zero, we obtain

$$\begin{aligned}&\frac{\partial f_0\left(\{\boldsymbol{\theta}_k\}_{k=0}^{K}, \tau_0\right)}{\partial \tau_0} = 0\\ &\Rightarrow \left(1+\frac{\tau_0 C}{(T-\tau_0)B}\right)\log\left(1+\frac{\tau_0 C}{(T-\tau_0)B}\right) = \frac{CT}{B(T-\tau_0)}.\end{aligned} \tag{49}$$

Denote $z_1 = 1 + \frac{\tau_0 C}{(T-\tau_0)B}$, thus, we have

$$\begin{aligned}&z_1 \log(z_1) - z_1 = \frac{C}{B} - 1\\ &\Rightarrow \log\left(\frac{z_1}{\exp(1)}\right)\exp\left(\log\left(\frac{z_1}{\exp(1)}\right)\right) = \frac{\frac{C}{B}-1}{\exp(1)}.\end{aligned} \tag{50}$$

Consider the relation $x_1 \exp(x_1) = y_1 \Rightarrow x_1 = \mathcal{W}(y_1)$ and with some mathematical manipulations, the optimal solution of $\tau_0$ can be derived as (13), which completes the proof of *Theorem* 3.

## REFERENCES


[1] M. D. Renzo, A. Zappone, M. Debbah, M. Alouini, C. Yuen, J. D. Rosny, and S. Tretyakov, "Smart radio environments empowered by reconfigurable intelligent surfaces: How it works, state of research, and road ahead," *IEEE J. Sel. Areas Commun.*, vol. 38, no. 11, pp. 2450–2525, Nov. 2020.

[2] C. Huang, S. Hu, G. C. Alexandropoulos, A. Zappone, C. Yuen, R. Zhang, M. Di Renzo, and M. Debbah, "Holographic MIMO surfaces for 6G wireless networks: Opportunities, challenges, and trends," *IEEE Wireless Commun.*, vol. 27, no. 5, pp. 118–125, Oct. 2020.

[3] Q. Wu and R. Zhang, "Towards smart and reconfigurable environment: Intelligent reflecting surface aided wireless network," *IEEE Commun. Mag.*, vol. 58, no. 1, pp. 106–112, Jan. 2020.

[4] X. Zhou, R. Zhang, and C. K. Ho, "Wireless information and power transfer: Architecture design and rate-energy tradeoff," *IEEE Trans. Commun.*, vol. 61, no. 11, pp. 4754–4767, Nov. 2013.

[5] R. Zhang and C. K. Ho, "MIMO broadcasting for simultaneous wireless information and power transfer," *IEEE Trans. Wireless Commun.*, vol. 12, no. 5, pp. 1989–2001, May 2013.

[6] B. Clerckx, R. Zhang, R. Schober, D. W. K. Ng, D. I. Kim, and H. V. Poor, "Fundamentals of wireless information and power transfer: From RF energy harvester models to signal and system designs," *IEEE J. Sel. Areas Commun.*, vol. 37, no. 1, pp. 4–33, Jan. 2019.

[7] H. Ju and R. Zhang, "Throughput maximization in wireless powered communication networks," *IEEE Trans. Wireless Commun.*, vol. 13, no. 1, pp. 418–428, Jan. 2014.

[8] Q. Wu and R. Zhang, "Weighted sum power maximization for intelligent reflecting surface aided SWIPT," *IEEE Wireless Commun. Lett.*, vol. 9, no. 5, pp. 586–590, May 2020.

[9] Q. Wu and R. Zhang, "Joint active and passive beamforming optimization for intelligent reflecting surface assisted SWIPT under QoS constraints," *IEEE J. Sel. Areas Commun.*, vol. 38, no. 8, pp. 1735–1748, Aug. 2020.

[10] C. Pan, H. Ren, K. Wang, M. Elkashlan, A. Nallanathan, J. Wang, and L. Hanzo, "Intelligent reflecting surface aided MIMO broadcasting for simultaneous wireless information and power transfer," *IEEE J. Sel. Areas Commun.*, vol. 38, no. 8, pp. 1719–1734, 2020.

[11] Z. Chu, J. Zhong, P. Xiao, D. Mi, W. Hao, J. Shi, and L. Yang, "Unlock self-sustainability of reconfigurable intelligent surface in wireless powered iot networks," *to appear in IEEE Commun. Mag.*, 2022.

[12] B. Lyu, P. Ramezani, D. T. Hoang, S. Gong, Z. Yang, and A. Jamalipour, "Optimized energy and information relaying in self-sustainable IRS-empowered WPCN," *IEEE Trans. Commun.*, vol. 69, no. 1, pp. 619–633, 2021.

[13] Z. Chu, P. Xiao, D. Mi, W. Hao, M. Khalily, and L.-L. Yang, "A novel transmission policy for intelligent reflecting surface assisted wireless powered sensor networks," *IEEE J. Sel. Topics Signal Process.*, vol. 15, no. 5, pp. 1143–1158, Aug. 2021.

[14] Q. Wu, X. Zhou, and R. Schober, "IRS-assisted wireless powered NOMA: Do we really need different phase shifts in DL and UL?," *IEEE Wireless Commun. Lett.*, vol. 10, no. 7, pp. 1493–1497, Jul. 2021.

[15] D. Zhang, Q. Wu, M. Cui, G. Zhang, and D. Niyato, "Throughput maximization for IRS-assisted wireless powered hybrid NOMA and TDMA," *IEEE Wireless Commun. Lett.*, vol. 10, no. 9, pp. 1944–1948, Sept. 2021.

[16] Q. Wu, X. Zhou, W. Chen, J. Li, and X. Zhang, "IRS-aided WPCNs: A new optimization framework for dynamic irs beamforming," *IEEE Trans. Wireless Commun.*, vol. 21, no. 7, pp. 4725–4739, Jul. 2022.

[17] S. Boyd and L. Vandenberghe, *Convex Optimization*. Cambridge, UK: Cambridge University Press, 2004.

[18] Z. Zhu, Z. Li, Z. Chu, G. Sun, W. Hao, P. Liu, and I. Lee, "Resource allocation for intelligent reflecting surface assisted wireless powered IoT systems with power splitting," *IEEE Trans. Wireless Commun.*, vol. 21, no. 5, pp. 2987–2998, May 2022.

[19] Z. Wang, L. Liu, and S. Cui, "Channel estimation for intelligent reflecting surface assisted multiuser communications: Framework, algorithms, and analysis," *IEEE Trans. Wireless Commun.*, vol. 19, no. 10, pp. 6607–6620, Oc. 2020.

[20] L. Wei, C. Huang, Q. Guo, Z. Yang, Z. Zhang, G. C. Alexandropoulos, M. Debbah, and C. Yuen, "Joint channel estimation and signal recovery for RIS-empowered multiuser communications," *IEEE Trans. Commun.*, vol. 70, no. 7, pp. 4640–4655, Jul. 2022.

[21] G. Zhou, C. Pan, H. Ren, K. Wang, and A. Nallanathan, "A framework of robust transmission design for IRS-aided MISO communications with imperfect cascaded channels," *IEEE Trans. Signal Process.*, vol. 68, pp. 5092–5106, Aug. 2020.

[22] S. Hong, C. Pan, H. Ren, K. Wang, K. K. Chai, and A. Nallanathan, "Robust transmission design for intelligent reflecting surface-aided secure communication systems with imperfect cascaded CSI," *IEEE Trans. Wireless Commun.*, vol. 20, no. 4, pp. 2487–2501, Apr. 2021.

[23] Y. Omid, S. M. Shahabi, C. Pan, Y. Deng, and A. Nallanathan, "Low-complexity robust beamforming design for IRS-aided MISO systems with imperfect channels," *IEEE Commun. Lett.*, vol. 25, no. 5, pp. 1697–1701, May 2021.

[24] Z. Chu, P. Xiao, D. Mi, W. Hao, Z. Lin, Q. Chen, and R. Tafazolli, "Wireless powered intelligent radio environment with non-linear energy harvesting," *to appear in IEEE Internet Things J.*, pp. 1–1, 2022.

[25] Y. Chen, N. Zhao, and M.-S. Alouini, "Wireless energy harvesting using signals from multiple fading channels," *IEEE Trans. Commun.*, vol. 65, no. 11, pp. 5027–5039, Nov. 2017.

[26] J. Song, P. Babu, and D. P. Palomar, "Sequence design to minimize the weighted integrated and peak sidelobe levels," *IEEE Trans. Signal Process.*, vol. 64, no. 8, pp. 2051–2064, Apr. 2016.

[27] Y. Sun, P. Babu, and D. P. Palomar, "Majorization-minimization algorithms in signal processing, communications, and machine learning," *IEEE Trans. Signal Process.*, vol. 65, no. 3, pp. 794–816, Feb. 2017.

[28] K. Alhujaili, V. Monga, and M. Rangaswamy, "Transmit MIMO radar beampattern design via optimization on the complex circle manifold," *IEEE Trans. Signal Process.*, vol. 67, no. 13, pp. 3561–3575, Jul. 2019.

[29] X. Yu, J.-C. Shen, J. Zhang, and K. B. Letaief, "Alternating minimization algorithms for hybrid precoding in millimeter wave MIMO systems," *IEEE J. Sel. Topics Signal Process.*, vol. 10, no. 3, pp. 485–500, Apr. 2016.

[30] M. Hua and Q. Wu, "Joint dynamic passive beamforming and resource allocation for IRS-aided full-duplex WPCN," *to appear in IEEE Trans. Wireless Commun.*, pp. 1–1, 2021.

[31] Z. Li, W. Chen, Q. Wu, H. Cao, K. Wang, and J. Li, "Robust beamforming design and time allocation for IRS-assisted wireless powered communication networks," *to appear in IEEE Trans. Commun.*, pp. 1–1, 2022.

[32] C. Pan, H. Ren, K. Wang, W. Xu, M. Elkashlan, A. Nallanathan, and L. Hanzo, "Multicell MIMO communications relying on intelligent reflecting surfaces," *IEEE Trans. Wireless Commun.*, vol. 19, no. 8, pp. 5218–5233, Aug. 2020.

[33] M. Hua, L. Yang, Q. Wu, C. Pan, C. Li, and A. L. Swindlehurst, "UAV-assisted intelligent reflecting surface symbiotic radio system," *IEEE Trans. Wireless Commun.*, vol. 20, no. 9, pp. 5769–5785, Sept. 2021.

[34] Q. Wu and R. Zhang, "Beamforming optimization for wireless network aided by intelligent reflecting surface with discrete phase shifts," *IEEE Trans. Commun.*, vol. 68, no. 3, pp. 1838–1851, 2020.